**Experimental Investigation of the Effect of NaCl Additive on the Formation and Evolution
of Particles in a Diffusion Flame**

by

Alireza Moallemi

A thesis submitted in partial fulfillment of the requirements for the degree of

Master of Science

Department of Mechanical Engineering
University of Alberta

Abstract

Formation and evolution of nano-particles in a laminar co-flow methane diffusion flame were investigated under two conditions: a pure methane flame and a methane flame doped with NaCl particles. Samples of nano-particles from different heights above the burner were extracted by a probe sampling system designed to dilute samples with very high dilution ratios. Subsequent to sampling, particles were directed to a scanning mobility particle sizer (SMPS) to measure the particle size distribution. The rapid thermocouple insertion method was utilized to measure the flame temperature at different locations. The structure of the nano-particles was investigated by thermophoretic sampling of particles from different heights above the burner and analyzing these samples with a transmission electron microscope (TEM). Using the SMPS scans and TEM images, different stages of nano-particles evolution, from inception to coagulation and oxidation, were observed. Results show that considerable concentrations of NaCl nano-particles emerge at low heights above the burner (8 mm) in the methane flame doped with NaCl particles. The NaCl nano-particles formed at lower heights above the burner disappear as the height above the burner increases. Additionally, by comparing the results obtained in the methane diffusion flame and the flame doped with NaCl, it was found that the addition of NaCl particles leads to the formation of particles with smaller sizes and greater concentrations in regions of the flame were coagulation is the dominant process of particle formation.

Preface

The experimental set-up that was employed in this study is an updated version of the experimental set-up used by Kazemimanesh et al. (2016). In Kazemimanesh et al. (2016), I was responsible for conducting the experiments and designing the sampling system in collaboration with Mohsen Kazemimanesh. I also wrote the introduction section. Other sections of that paper were written by Mohsen Kazemimanesh.

Due to the similarities between the experimental set-ups used in Kazemimanesh et al. (2016) and this study, some of the passages that are included in the second and third chapters of this thesis are extracted from Kazemimanesh et al. (2016). Parts of Chapter 2 including the introduction section, co-flow burner, aerosol measurement suit and dilution ratio measurements sections and parts of chapter 3 which are related to the effect of dilution ratio on particle size distribution are based on Kazemimanesh et al. (2016). Additionally, components of the experimental set-up including the co-flow burner and PID controller used in the sampling system were designed by Mohsen Kazemimanesh.

The thermophoretic sampler used for collecting particle samples on TEM grids was provided by Dr. Steve Rogak and is a property of University of British Colombia. TEM samples were analyzed in cell imaging facility in the Department of Oncology at University of Alberta. The TEM microscope facility was supervised by Dr. Xuejun Sun and several TEM and HRTEM images that are included in this thesis were taken by Dr. Sun.

To Mahin, Noorollah, and Shima

Acknowledgements

I would like extend my sincere appreciation to Dr. Jason Olfert whose assistance and guidance as my supervisor made it possible for me to overcome challenges of this project. His ideas had a great impact on the improvements of this research. Dr. Olfert was a source of inspiration and always motivated me to do my best and never get disappointed upon facing difficult challenges during the experiments.

I would like to also express my gratitude towards my co-supervisor, Dr. Larry Kostiuk. His passion and enthusiasm to solve different challenges faced during the course of research were one of the main driving forces of this project. Without Dr. Kostiuk's astute advice and comments, this project could have never come to fruition.

I want to also thank Mohsen Kazemimanesh who patiently assisted me through different stages of the project and had a vital contribution on the construction and improvement of different components of the experimental set-up.

I would like to thank Dr. Steve Rogak from University of British Columbia for providing us with the thermophoretic sampler that was one the essential equipments to complete this work. Additionally, I want to thank Ramin Dastanpour and Rene Zepeda for instructing us on how to utilize the thermophoretic sampler. I want to thank Dr. Sun from the Department of Oncology at University of Alberta who helped us with analyzing samples with TEM and instructed us on how to work with TEM. Additionally, I want to thank Kurtis Broda who helped me with running the CPMA.

Finally I would like to thank my family and friends who encouraged and supported me during my graduate program.

Table of Contents

List of Tables

List of Figures

Nomenclature

List of Symbols

A	Surface area of thermocouple (m^2)
c_p	Specific heat of thermocouple (kJ/kg $\cdot$ K)
d	Thermocouple junction diameter (m)
d_m	Mobility diameter of particles (nm)
$\dfrac{dN}{dlog(d_m)}$	Normalized number density (cm^{-3})
ε	Emissivity
$\bar{h}$	Enthalpy (kJ/kmole)
$\bar{h}_f^{\circ}$	Enthalpy of formation (kJ/kmole)
k	Gas conductivity (W/m $\cdot$ K)
MW	Molecular weight (kg/kmole)
$m(d_m)$	Mass mobility function (fg)
M	Mass concentration (fg)
$\dot{m}$	Mass flow rate (SLPM)

μ_g	Dynamic viscosity of gas at gas temperature (Pa.s)
μ_{th}	Dynamic viscosity of gas at thermocouple surface temperature (Pa.s)
$\dot{N}$	Mole flow rate (mole/min)
N	Number of mole (kmole)
Nu	Nusselt number
P	Pressure (Pa)
Pr	Prandtl number
σ	Stefan–Boltzmann constant (W/m$^2 \cdot$ K^4)
$\dot{Q}_{rad}$	Radiative heat transfer (kJ)
$\dot{Q}_{conv}$	Convective heat transfer (kJ)
$\dot{Q}_{cond}$	Conductive heat transfer (kJ)
$\dot{Q}_{cat}$	Heat transfer due to catalytic reactions (kJ)
Re	Reynolds number around thermocouple
t	Sampling time (s)

τ	Time constant (s)
T_{th}	Thermocouple temperature (K)
T_{g}	Gas temperature (K)
T_{w}	Temperature of the enclosing surface (K)
V_{th}	Volume of the thermocouple bead (m^3)
X	Mole Fraction

List of Acronyms

CMD	Count Median Diameter
CPC	Condensation Particle Counter
CPMA	Centrifugal Particle Mass Analyzer
DMA	Differential Mobility Analyzer
DR	Dilution Ratio
GC	Gas Chromatography
HAB	Height above the Burner
HACA	Hydrogen Abstraction C$_2$H$_2$ Addition

HEPA	High Efficiency Particulate Arrestance
HRTEM	High Resolution Transmission Electron Microscope
ID	Inside Diameter
LII	Laser Induced Incandescence
NIST	National Institute of Standard Technology
OD	Outside Diameter
PAH	Polycyclic Aromatic Hydrocarbon
PID	Proportional Integral Derivative
PSD	Particle Size Distribution
SLPM	Standard Liters Per Minutes
SMPS	Scanning Mobility Particle Sizer
TEM	Transmission Electron Microscope
TPS	Thermophoretic Sampler
USGS	United States Geological Survey
VOC	Volatile Organic Compounds

WHO   World Health Organization

Chapter 1

Introduction

1.1 Flaring

In the oil and gas industry flaring is a conventional method for disposing unwanted combustible gases. Flares are typically flames burning in the open air and their main purpose is to transform the unwanted gases to more desirable products prior to dispersing them to the atmosphere. There are three different types of flares in the oil and gas industries categorized by their application: emergency flares, process flares and production flares (Johnson et al. 2001). In the oil and gas industry, the sector that is related to exploration and extraction of gas and petroleum is referred to as upstream oil and gas industry, and the sector which deals with refining and processing gas and petroleum is referred to as downstream oil and gas industry (Schweitzer 2010).

Emergency and process flares are used in the downstream oil and gas industries. In large petrochemical facilities emergency flares are employed when it is required to burn a significant volume of gas in a short period of time for safety of personnel or infrastructures (Johnson et al. 2001; McEwen & Johnson 2012).

In downstream oil and gas facilities, process flares are typically used for discarding leaked gases from process lines, and therefore involve flaring relatively small volume flow rates of gases in a continuous manner (Johnson et al. 2001).

Production flares are employed in the upstream oil and gas industries. In the gas industry at the early stage of well production, these types of flares are commonly used to discard large volumes

1

of gases (Johnson et al. 2001). Production flares are also used in the oil industry for discarding the unwanted gases that are produced during the process of extraction (Johnson et al. 2001).

During the process of the recovery and handling of crude oil, some gas by-products are produced, which are referred to as *associated gas or solution gas* (Johnson & Coderre 2011). Associated gas is naturally dissolved in the liquids (petroleum and brackish water), and once the temperature and pressure decreases during extraction, the associated gas is released (Johnson et al. 2001). After bringing the combination of petroleum and brine to the surface, it is directed to the separation facilities to separate petroleum from other by-products, including the water content, which mostly consists of brine, and associated gases. Associated gas is mostly composed of methane and other short-chain hydrocarbons (Weyant et al. 2016). If the associated gas is not economically justifiable to use, the associated gas is treated as an undesirable by-product of petroleum extraction and is discarded. There are two major methods for disposing of associated gas: venting and flaring. In the venting process, unburned gas is directly emitted to the atmosphere, while in flaring, associated gas is combusted prior to atmospheric release.

Methane is the most abundant species in associated gas and it is one of the major contributors to global warming. In a 100 year time scale methane is about 25 times more potent than CO_2 for global warming (Solomon et al. 2007); thus, the impact of venting on global warming is more severe than flaring. Although flaring reduces the risk of global warming, the combustion efficiency of flares is not 100% and other byproducts of incomplete combustion such as such as soot particles (black carbon) could be emitted by flaring associated gases. It was approximated that the global volume of gas being flared in the upstream oil and gas industry in 2012 is 129 billion m^3 (Elvidge et al. 2016), and compared to flaring in downstream oil and gas industries, upstream flaring is the greater source of gas flaring (Elvidge et al. 2016). Alberta is known to be

2

the main source of flaring in Canada (McEwen 2010). Based on the upstream petroleum industry flaring and venting report in 2014 the amount of associated gas flared from crude oil and crude bitumen batteries in the Province of Alberta was 490 million m^3 and the amount of flaring from other sources (gas batteries, well testing, gas plants and gas gathering systems) was 550 million m^3 (Alberta Energy Regulator 2016).

Amongst all of the byproducts of incomplete combustion, soot is considered one of the major contributors to global warming along with carbon dioxide (Sato et al. 2003; Bond & Sun 2005). It has been approximated that about 4% of the total world-wide black carbon emission is due to flaring (Fawole et al. 2016; Weyant et al. 2016). Additionally, flaring is considered as one of the prime source of black carbon deposition on the Arctic ice (Stohl et al. 2013), which is believed to affect the arctic climate.

1.2   Hydraulic Fracturing and Fracking Fluid

During the past decade, the extraction of gas and oil from unconventional formations such as low-permeability organic-rich shale formations and tight-sand reservoirs has increased due to improvements in horizontal drilling and employment of hydraulic fracturing (Vengosh et al. 2014). In the hydraulic fracturing process fracturing fluid is injected into the wellbore. Injection of fracturing fluid increases the pressure and creates fractures in rock formations in the reservoir. Fractures created in rocks increase the permeability of the formation and improve the extraction rate of oil and gas from the reservoir (Kazemimanesh 2014). A schematic of the final state of a fractured reservoir is shown in Figure 1.1 (based on (Barbot et al. 2013)). After fracturing, the oil or gas is extracted, but these results in carrying a mixture of brine and fracturing fluid to the surface.

Currently, hydraulic fracturing is used extensively to improve oil and gas extraction and it has been proposed that 60% of the wells that have been drilled (worldwide) are subjected to hydraulic fracturing over the last decade (Miller et al. 2013).
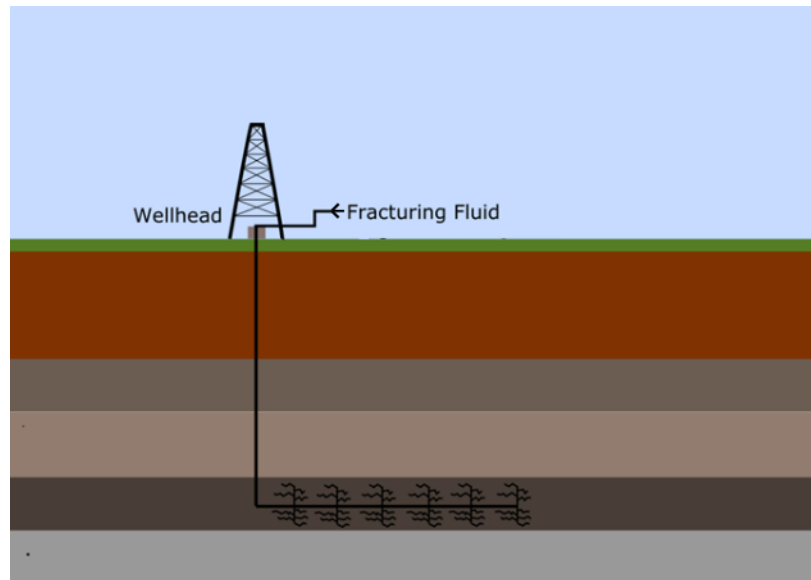
Figure 1.1. A schematic of hydraulic fracturing in a horizontal wellbore (based on Barbot et al. 2013)

1.3   Flowback and Produced Water

The flow returning to the well is either categorized as "flowback water" or "produced water". Flowback water is the fluid which returns to the surface once the hydraulic fracturing of the well is over (Barbot et al. 2013). Flowback water returns to the surface within the first two weeks after the hydraulic fracturing process (Haluszczak et al. 2013). Produced water is the fluid returning to the surface after the production phase of the well has started (Barbot et al. 2013). The flow returning from the well has a high concentration of inorganic minerals (Haluszczak et al. 2013).

Chemical compositions of both flowback and produced water have been extensively investigated in several papers and reports. Chemical composition and concentration of chemical species were measured for flowback and produced water for different formations such as the Marcellus shale formation (Haluszczak et al. 2013; Barbot et al. 2013; Chapman et al. 2012; Ziemkiewicz & Thomas He 2015; Horner et al. 2011; Hayes & Severin 2012; Gregory et al. 2011), Barnett (Horner et al. 2011), Woodford (Acharya et al. 2011) and Horn River (Paktinat et al. 2011). Also, the United States Geological Survey (USGS) National Produced Waters Geochemical Database includes the compositions of produced water samples gathered from different formations (Blondes et al. 2014). Additionally, some studies inspected temporal changes of flowback water composition and concentration of major species. Figure 1.2 shows the changes in chlorine and sodium for two representative flowback water samples from the Western and Eastern United States (McElreath 2011). These samples were gathered within 30 days following the hydraulic fracturing of wells. The results from that study and other similar studies (Barbot et al. 2013; Zolfaghari Sharak et al. 2014) suggest that generally the concentration of the non-organic compounds in flowback water increases as time goes on. As the production of a fracked well continues, most of the water that was initially used in the fracturing fluid returns to the surface within the first weeks of the fracturing process. Therefore, the volume of water derived from the fracturing fluid gradually decreases. Subsequently the concentration of mineral compounds in the water returning to the surface increases and approaches the composition of the native fluid in the reservoir (McElreath 2011).
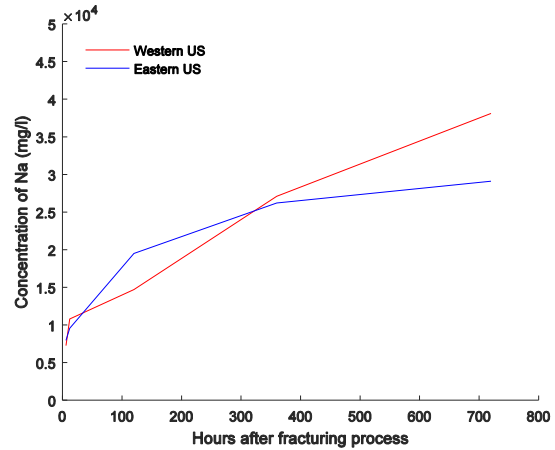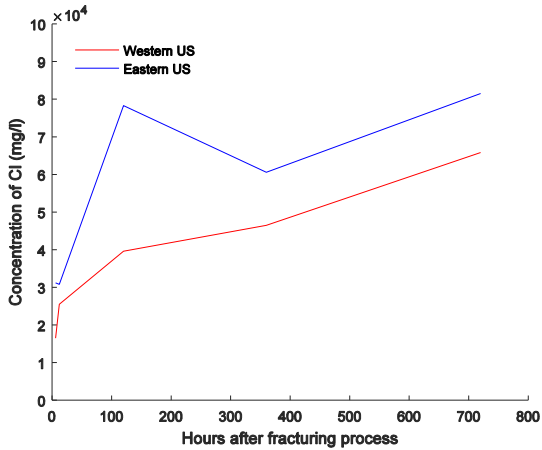
(a) Cl concentration changes after fracturing   (b) Na concentration changes after fracturing

Figure 1.2 Na and Cl concentration changes in Western and East US samples of flowback water after fracturing (McElreath 2011)

Most research papers related to produced water are only focused on the chemical composition from a specific geographical region. The United States Geological Survey National Produced Waters Geochemical Database v2.1 (Blondes et al. 2014) provides information on the composition of produced waters sampled from different regions of the United States. By analyzing USGS database (see Appendix A) the following representative[1] composition for produced water was determined and is shown in Table 1.1.

---

[1] The representative chemical composition is based on the median of the concentration of chemicals from produced water of different wells across the US. The whole procedure for obtaining this representative composition is included in Appendix A.

Table 1.1. Median concentration of prominent chemical compounds of the representative produced water solution from USGS database

Elements	Concentration (mg/l)
Cl	178,000
Na	91,200
Ca	11,300
CHO_3	300
SO_4	1000
K	2300
Mg	1400

As it can be noticed the most abundant component of the produced water are Na and Cl. Other studies (Miller et al. 2013; Barbot et al. 2013; Slutz et al. 2012; McElreath 2011) have confirmed that Na and Cl are the most abundant elements in the produced and flowback water solutions from different regions of the US.

1.4 Flares and Produced Waters

Oil and produced water extracted are collected in oil batteries in order to separate produced water from the oil. It is possible, that during the separation process some liquid droplets, could find their way into the flare stack and be burned along with the flare gases (Kazemimanesh 2014). One of the objectives of the current project is to investigate the effect of Na and Cl as the most prominent species in produced water, on formation of particles in flares.

1.5 General Discussion on Soot

As flaring is one of the main sources of soot emission to the atmosphere, it is important to review the risks associated with soot particles and how significant of an impact would soot emissions pose to human health and the environment. Additionally, it is important to become familiar with

the processes associated with the formation and evolution of soot particles within flames, since the first step toward mitigation of soot emission is to understand its origin.

1.5.1   Environment and Health impact of Soot particles

Ultrafine soot particles (below 100 nm) emitted from combustion sources can have a significant impact on human health. These types of particles usually have a fractal-like structure, which is an aggregate of several spherical primary soot particles with diameters of the order of tens of nanometers. Due to their fractal-like structure, ultrafine soot particles have a large surface area to mass ratio which could promote considerable surface reactions on these particles (Abid 2009). It has been estimated that 3 million deaths in 2012 (worldwide) were provoked by cancer, cardiovascular and respiratory diseases due to sub 10 µm airborne particles (WHO 2016). The typical size range of soot emitted to the atmosphere from automotive emissions is between 10 nm to 100 nm, and for particles that are in this size range the settling velocity is very low which means that these soot particles could remain airborne for long periods of time (Abid 2009). Inhaled ultrafine particles (sub 100 nm particles) could enter into the respiratory system and could be transported to the central nervous (Oberdörster et al. 2004) and cardiovascular systems (Pedata et al. 2013).

In addition to health hazards, soot emissions from combustion sources are one of the major contributors to the global climate change. Soot is considered the second or third major contributor to global warming after CO_2, and with a similar magnitude as methane (Bond & Sun 2005). The major role of soot on global warming is attributed to its physical property of being a potent absorbent of visible light (Bond & Sun 2005). Soot particles can influence global climate through several pathways. Soot particles are strong light absorptions and these particles in

droplets and ice crystals that form the clouds can change the planetary albedo[2] (Abid 2009). It was shown that black carbon could influence regional climate and could be a possible reason for the precipitation trends in China throughout the last decades which have caused an increase in rain fall in southern regions and drought in northern regions of China (Menon et al. 2002). One of the most sensitive regions on the planet that has been affected by global warming is the Arctic. Researches have shown that the rate of warming in the Arctic is faster than other region of the globe (Koch & Hansen 2005). The deposition of black carbon on snow and ice in the arctic could increase the surface warming at these regions (Ramanathan & Carmichael 2008). Simulations have suggested that 42% of the annual surface concentration of black carbon in the arctic is due to flaring (Stohl et al. 2013), which could point to flaring as one of the major contributor of arctic climate change.

1.5.2 Soot Formation and Evolution

Since soot emission from combustion sources has an undeniably significant impact on human health and global environment it is necessary to investigate the origin of soot particles. Over the last thirty years numerous studies were conducted (Haynes & Wagner 1981; Santoro et al. 1983; 1987; Frenklach & Wang 1991; Dobbins et al. 1998; Siegmann et al. 2002; Zhao et al. 2003b; Wang 2011) on different flames and fuels to understand the origin of soot and develop mechanisms that can explain the formation of soot particles in flames. Although, researches shed light on different aspects of soot formation and evolution, there are still some speculations regarding these phenomena.

---

[2] Albedo is the portion of light reflected back from and object and is an indication of how bright and object is.
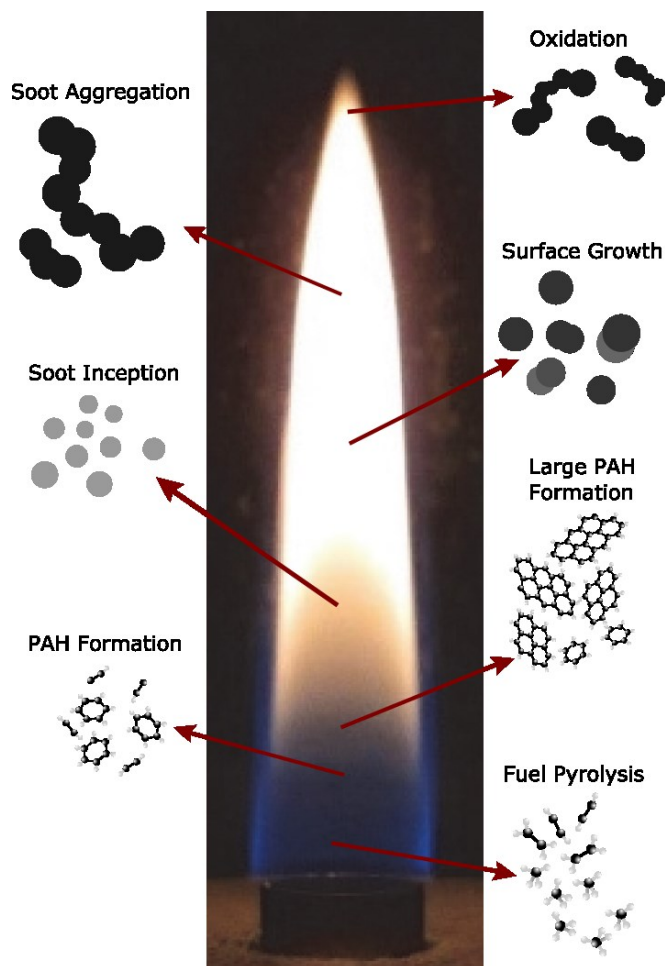
Figure 1.3. A scheme of the evolution of soot particles from inception to oxidation (picture inspired from (Kholghy 2012; Michelsen 2016)).

Figure 1.3 shows different stages of soot formation in a simple laminar jet diffusion flame with co-flowing air. Soot is a product of incomplete combustion. Polycyclic aromatic hydrocarbons (PAHs) are considered as the main precursor to soot (Frenklach 2002); thus, formation of the first aromatic ring is a critical step in the soot nucleation process. Soot formation is highly related to concentrations of acetylene, hydrogen and the temperature of the flame (Wang 2011). As it is shown in Figure 1.3 during the early stages of combustion some intermediate species are formed. Acetylene is one of the most abundant intermediate species in flames (Wang 2011)

which has a great contribution to the formation of the first aromatic ring (Frenklach 2002). Hydrogen acts as the catalysts and flame temperature controls the kinetics of reactions (Wang 2011). It was suggested that reactions between propargyl and acetylene could be the most dominate reaction that leads to the formation of the first aromatic ring (Frenklach 2002). It has also been suggested that PAHs are formed and grow through hydrogen abstraction and C_2H_2 addition (HACA) mechanism (Frenklach & Wang 1991). HACA is a continual reaction sequence (Frenklach 2002) which consists of abstraction of hydrogen atoms from aromatic molecules which would transform the aromatics into radicals. The aromatic radicals react with acetylene molecules. As the reaction between acetylene and aromatics continues new aromatic rings would be added to the initial aromatic molecules and the size of PAHs grow. It should be noted that HACA is based on reversible reactions and it is a function of temperature (Kholghy 2012). PAHs formed by the HACA mechanism combine and create incipient soot particles. The carbon to hydrogen ratio in incipient soot particles are 1.4 - 2.5 (Michelsen 2016). Transmission electron microscopy and atomic force microscopy confirm that incipient soot particles have spherical and liquid like structures (Michelsen 2016).

The particle growth process is accompanied by a loss in hydrogen content of soot particles and solidification (Michelsen 2016). As soot particles become more mature the carbon to hydrogen ratio grows to about 10 (Howard 1991; Michelsen 2016). The collision of mature soot particles due to Brownian motion (a process called coagulation) is another process that contributes to the size growth of soot particles and results in the formation of chain-like soot aggregates. Coagulation of soot particles will increase the size of particles but at the same time reduce the total number concentration. Another critical process that can affect the evolution and morphology of soot particles is oxidation. During oxidation, soot particles react mainly with OH

and O_2 (Kholghy 2012). The oxidation process is dominated by OH in fuel rich regions of a flame while in fuel lean regions O_2 is the dominant oxidizer (Kholghy 2012). Oxidation reduces the size and number density of soot particles.

Contaminating the fuel with additives could influence the processes that control soot formation either through chemical pathways or by affecting the temperature (Ni et al. 1994). As mentioned earlier it is possible for produced water to get transported to the flare stack. Based on the composition of produced water (Table 1.1) Na and Cl are the prominent elements in produced water. Thus, NaCl could affect the processes involved in soot formation of associated gas flares. The effect of different alkali and alkali earth additives on formation of soot particles have been studied for over three decades (Haynes et al. 1979; Bonczyk 1988; Mitchell & Miller 1989; Tappe et al. 1993; Glarborg 2007; Di Stasio et al. 2011). It has been shown that the addition of alkali metals to different types of flames with different fuels could result in a reduction of soot volume fraction and increases the number density of soot particles; however, speculations continue regarding the mechanisms that affect soot formation.

1.6   Objectives of Thesis

The principal objectives of this project is to shed light on the evolution of nano-particle formation (soot or other compounds) in a laminar co-flow methane-air diffusion flame as a small scale representation of an associated gas flare and to investigate the potential effects that NaCl additives could induce on nano-particle formations. The first step toward achieving these objectives was the design and construction of a burner that could generate a laminar jet diffusion flame as a source of aerosol and a NaCl injection system than can introduce NaCl particles into the burner. The subsequent step was to design an aerosol extractive sampling system able of

operating under the extreme conditions of a diffusion flame created by the burner and preserve the integrity of aerosol samples. The next step was to transfer samples from different locations of the flame to a scanning mobility particle sizer (SMPS) and measure the size distribution of soot particles formed in a pure methane flame and a flame doped with NaCl. As formation of nano-particles such as soot is remarkably temperature dependent, a method was needed to measure the flame temperature and produce flame temperature profiles. Finally, the morphology of soot particles, from the structure of soot particles at early stages of surface growth to mature soot particle were probed by analyzing samples from different regions of the flame with transmission electron microscopy (TEM). Below is a summarized list of the main objectives in this study:

- Design, construct and deploy a probe sampling system for aerosol extraction from a Santoro burner diffusion flame which flexible range of sample dilution ratios

- Perform particle size distribution measurements by using scanning mobility particle sizer (SMPS) at different heights above burner (HAB) of a laminar pure methane flame and methane flame doped with NaCl particles

- Design, construct and deploy thermocouple measurement for obtaining the temperature profile of the pure methane flame and methane flame doped with NaCl particles

- Design, construct and deploy a grid sampling system for the transmission electron microscopy on aerosol samples gathered from different HABs of the flame from both pure methane flame and doped methane flame with NaCl particles

- Determine the possible effect of NaCl addition on soot morphology and evolution

1.7   Outline of Thesis

In Chapter 2 all the components that were used in the experiments are described. To investigate the formation of nano-particles such as soot, a co-flow burner is employed to create a laminar methane diffusion flame as the source of nano-particles. A probe sampling system was designed and constructed to extract samples and highly dilute them upon sampling. The sampling system and the method used for quantitatively measuring the amount of dilution of the sample are explained. The measurement of soot particle size distributions was conducted by a scanning mobility particle sizer (SMPS). Additionally, a temperature measurement system that enabled insertion of thermocouple into specific locations inside the flame is described. The last component explained in Chapter 2 is the NaCl injection system which was designed to add NaCl particles to the fuel stream.

In Chapter 3, temperature profiles obtained in different heights of the flame is included and the effect of probe on flame temperature along the flame centerline was also investigated. The evolution of particle size distribution along the centerline of the flame was obtained. The effect of NaCl on nano- particle formation is investigated by comparing the result of soot evolution in both cases of pure methane flame and methane flame doped with NaCl particles. Finally, the morphology of nano-particles was studied by extracting samples from different locations of the flame in both cases of pure methane flame and methane flame doped with NaCl and analyzing the samples with a transmission electron microscope (TEM).

In Chapter 4 a summary of all the conclusions made in previous chapter is included.

Chapter 2

Experimental Set-up and Methodology

2.1   **Introduction**

The formation and morphology of soot particles form the early stages of soot inception to surface growth and coagulation in different types of flames have been extensively investigated during the past three decades. Several different methods are used for these investigations, which could be divided into two categories: non-intrusive and extractive techniques.

Non-intrusive techniques rely on the interaction between light and soot particles and require optical instruments to detect, and models to interpret, these interactions as physical properties of soot particles (Giechaskiel et al. 2014). Examples of these methods include laser light extinction, laser induced florescence, laser induced incandescence, and small angle X-ray scattering.

Of these methods, laser induced incandescence (LII) is currently one of the more popular laser-based techniques for soot particle measurements. This method has been employed for about three decades (Dasch 1985; Shaddix & Smyth 1996; Snelling et al. 2004; Crosland et al. 2011). In LII, the temperature of soot particles is increased by laser beam pulses to significantly higher temperatures (~ 4000 K) than the background temperature (Simonsson et al. 2016). The increase in temperature results in increased radiation from the particles which decreases in few nanoseconds later as the temperature of the heated particles returns to the surrounding temperature (Krüger et al. 2005). By analyzing the decaying radiation energy from particles, properties such as soot volume fraction can be inferred (Giechaskiel et al. 2014). LII does not significantly disturb the combustion source compared to probe sampling techniques but it

normally needs to be calibrated with other techniques such as laser light extinction and it is mostly used for measuring volume fraction of partially graphitized soot or fully mature soot particles (Michelsen 2016). LII allows for spatially resolved measurements; however, the laser energy can alter or destroy the structure of incipient soot particles (Abid 2009; Vander Wal et al. 1995). More details regarding other laser based techniques can be found elsewhere (Michelsen 2016; Giechaskiel et al. 2014).

Extractive techniques have been extensively used to investigate soot formation in combustion processes. One such technique is probe sampling, which has been employed for soot measurements from flames during the last few decades. This method offers the advantage of extracting samples directly from a known location in the flame and then using standard aerosol instruments to perform the measurement; however, concerns exist as to whether the measured sample is representative of that in the flow due to the presence of the probe in the flame (such as stagnation effects) and remains representative during the handling of the sample in tubing prior to measurement. Concerns during the handling of the sample include coagulation if the particle concentration is high and remains undiluted, and particle loss due to interception with tube walls.

Soot formation and its evolution have been investigated by Burtscher et al. (1993) on a natural gas diffusion flame and Hepp and Siegmann (1998) on a methane-argon diffusion flame. These groups used quartz micro probes that consisted of a tiny capillary for extracting soot particles and then diluting them with an inert carrier gas. Differential mobility analyzers and aerosol electrometers were used to obtain particle size distributions at different heights above the burner. Kasper et al. (1997) employed a stainless steel tube with a tiny pinhole that had a dilution flow of nitrogen and then measured particle size distributions using a scanning mobility particle sizer (SMPS) from a methane-argon diffusion flame doped with metallic additives. By using this type

of probe, the particles extracted from the flame were rapidly diluted and cooled by the flow of nitrogen. Higgins et al. (2002) used a similar sampling probe as Kasper et al. (1997) to investigate the oxidation rate of soot particles generated from an ethylene diffusion flame over a range of temperatures.

Probe sampling was also used extensively to investigate soot formation in premixed flames (Maricq et al. 2003; Zhao et al. 2003b; Maricq & Xu 2004; Zhao et al. 2005; Abid et al. 2008; Camacho et al. 2015). In some studies, the sampled soot particles were diluted in multiple stages to reach a high overall dilution and then directed to the particle measuring instruments (Maricq et al. 2003; Maricq & Xu 2004; Maricq 2011; Maricq 2012). Multi-stage dilution systems have the advantage of decreasing particle concentrations to within the measuring range of particle measurement instruments; however, such systems lack very high immediate dilution of the sample, which could possibly result in changing the particle size distribution if particle concentrations are very high at a sample point in the flame. Zhao et al.(2003b) improved and characterized a sampling technique similar to the technique used by Kasper et al. (1997) which enabled them to increase and alter the magnitude of sample dilution. The method of Zhao et al.(2003b) was used extensively to extract soot samples from ethylene premixed flat flames. Other studies have used a similar probe sampling method with multi-stage dilution for the study of nanoparticles in liquid fuel diffusion flames (Maricq 2011; 2012).

An extractive technique was employed in this project and samples were extracted directly from regions inside the flame. The following sections are focused on the different components of the experimental set-up and sampling probe.

2.2 Experimental Set-up

In this study the experimental set-up consists of a co-flow diffusion flame burner, a variable-dilution-ratio sampling system, a temperature measurement system, Thermophoretic sampler, particle measurement suite, NaCl injection system. Figure 2.1 shows the experimental set-up and its different components.
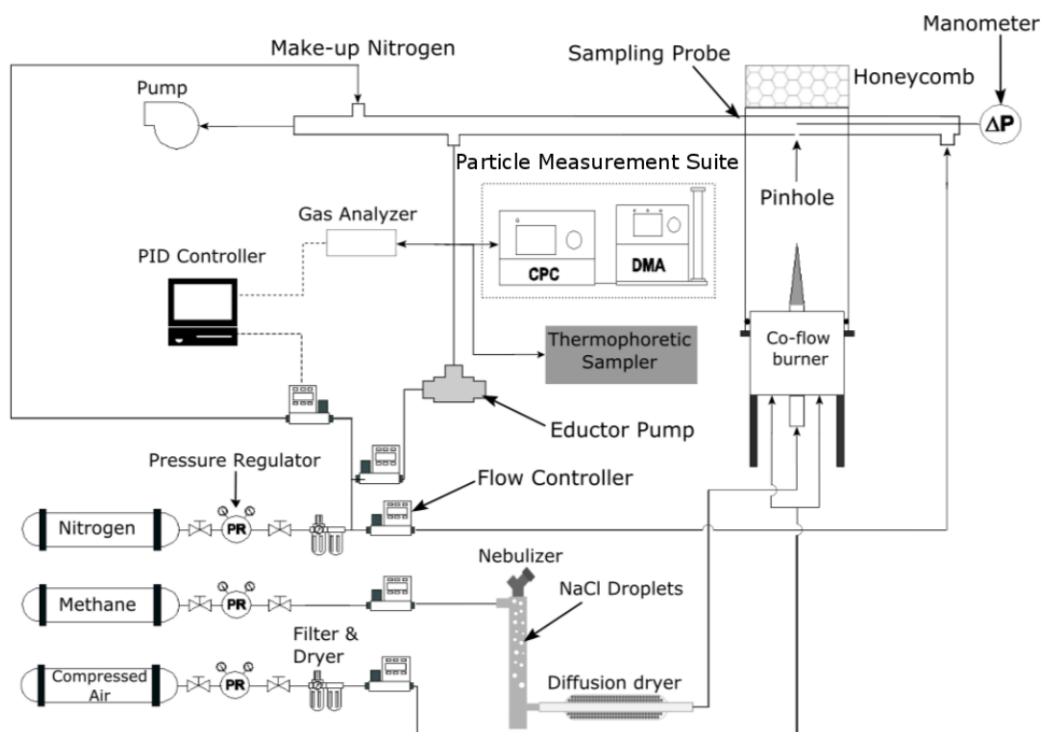
Figure 2.1. A scheme of the experimental set-up used in this study where ΔP the pressure difference between is ambient and a location near the pinhole inside the sampling probe. CPC (condensation particle counter) and DMA (differential mobility analyzer) are part of the particle measurement suite and are explained in the following sections. PR is pressure regulator.

2.2.1   Co-flow Burner

The burner used in this study is a co-flow laminar diffusion flame that was introduced and characterized by Santoro et al. (1983) for different types of fuels such as ethylene and methane. Exploded and cross section views of the co-flow burner are shown in Figure 2.2.

(a)   (b)
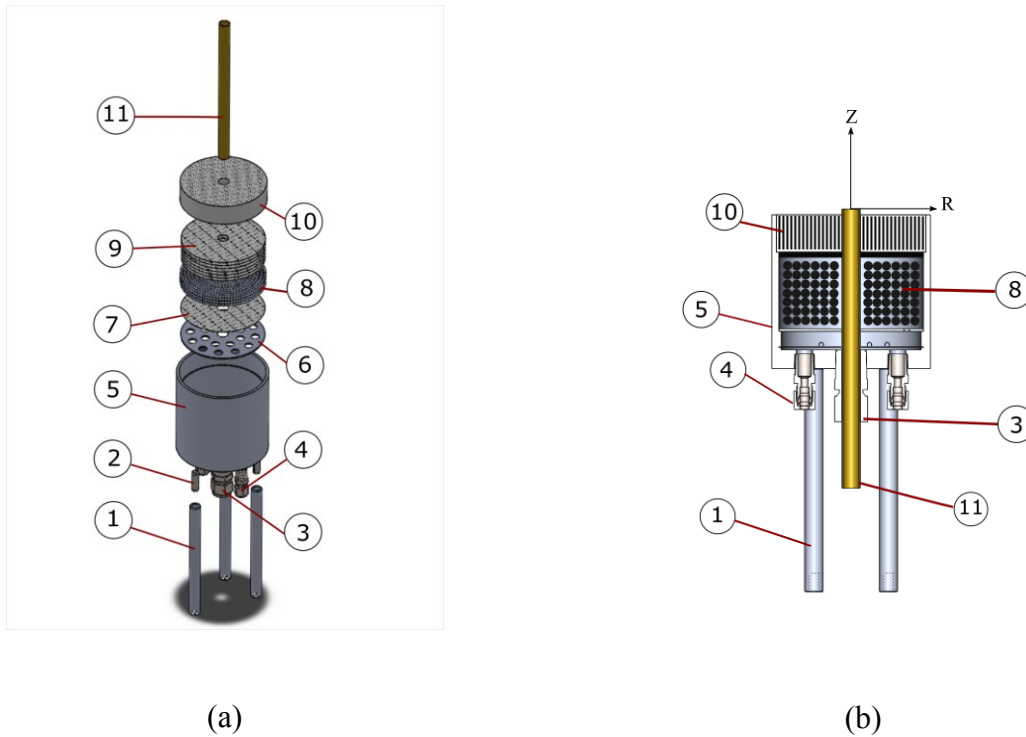
1. Burner stand

2. Spring pin

3. Fuel inlet fitting

4. Air inlet fitting

5. Burner outer body

6. Air stabilizer plate

7. Single cupper mesh plate

8. Glass bead

9. Multiple cupper mesh plates

10. Ceramic honeycomb

11. Fuel tube

Figure 2.2. (a) Exploded view, (b) cross section view of co-flow burner.

This burner consists of two concentric tubes with ID dimensions of 101.6 mm and 11.1 mm. The central tube is made of copper while the outer tube is made of aluminum. Fuel flows through the central tube and air flows through the co-annular section of the burner. This design is intended to produce a stable flame by separating the reaction zone from quiescent air that has a shear layer and buoyancy interactions that cause the flame to flicker. To make the air flow uniform, the lower portion of the air passage is filled with 3.0 mm glass beads along with several copper mesh screens. The remaining section of the air flow passage that leads to the atmosphere is filled with a ceramic honey comb. To further stabilize the flame a quartz shield surrounds the burner and a ceramic honeycomb was placed at the top of the quartz shield. Figure 2.3 shows another view of the burner with glass shield and honeycomb. The shield consists of two pieces of half cylinder quartz glass with radius of 75 mm and a height of 300 mm that were placed on a mounting plat which was fixed by set screws to the burner body. Two O-rings were placed between the shields and burner body and the shields were fixed to the burner by clamps. The two piece quartz shield provides two vertical slots that allow the probe to move along the z-axis. It was mentioned in a previous study (Saffaripour et al. 2011) on a similar co-flow burner, the shield prevents the flame from being disturbed by movements of room air and that the ceramic honeycomb hinders the air circulation inside the shielded volume. The burner was mounted on two translation stages with the accuracy of 0.03 mm for adjusting the horizontal position of the burner tube.
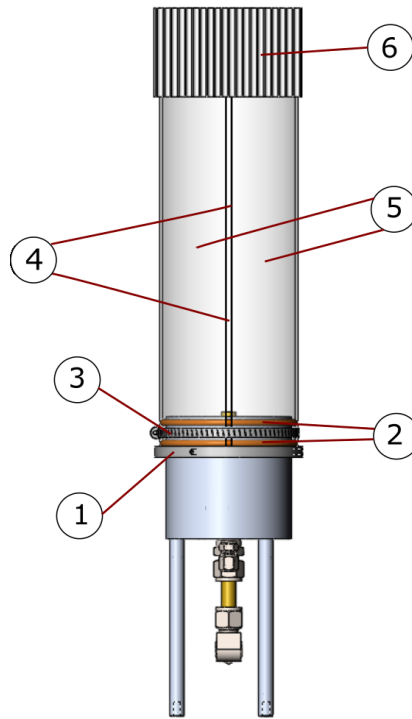
1. Mounting plate   2. O-rings

3. Clamp   4. Slot

5. Quartz Shield   6. Ceramic honeycomb

Figure 2.3. Shielded Santoro co-flow burner

In this study the flow rate of co-flow air and methane were 70.0 and 0.35 SLPM (standard liters per minute at 25°C and 1 atm), respectively, as this created a very stable flame. For maintaining these flow conditions a Cole-Parmer flow controller (Model 32907-71) was utilized for controlling the methane flow and the air flow was adjusted by an Omega flow controller (Model FMA-774A). The aforementioned flow rates for air and methane creates a laminar diffusion

flame with an approximate height of 60 mm. Figure 2.4 shows the laminar methane diffusion flame that was generated.

Figure 2.4. Laminar co-flow methane diffusion flame used in this study

2.2.2 Sampling System

In this study two types of probe sampling systems were used to extract samples from the flame in diluted and undiluted conditions. The undiluted sampling system was employed for CO_2 concentration measurements while the diluted sampling system was used for particle size distribution measurements, TEM sampling and CO_2 concentration measurements.

2.2.2.1 Diluted Sampling System

To maintain the integrity of the extracted samples, further reactions involving the particles and the interactions between particles (particle-particle coagulation) in the sampling line must be minimized, thus it is required to quench and dilute the extracted samples as soon as possible. It is commonplace to dilute the samples in the sampling line to prevent particle-particle coagulation

and chemical reactions. The dilution process could be done in either several separate stages (Maricq 2012; Gröhn et al. 2014) or it could be done in a single stage (Zhao et al. 2003b; Zhao et al. 2005; Abid et al. 2008; Sgro et al. 2009; De Filippo et al. 2009; Camacho et al. 2015). For this study samples were diluted several thousand times by N_2 in a single stage of dilution and sent to the particle measurement suite. A single stage dilution system dilutes samples to extreme extents upon extraction of the samples and prevents further coagulation in the sampling line. Figure 2.1 shows the diluted sampling system with the burner and aerosol measurement suite.

One of the main components of the diluted sampling system is the sampling probe which is used for extracting samples from the flame. The probe is a stainless steel tube (3.2 mm OD and 3.1 mm ID) with a pinhole in the middle that was positioned horizontally above the flame while the pinhole was facing downward. A flow of nitrogen is directed through the probe and samples where extracted through the pinhole. The sampling system was mounted on a separate motor-driven translational stage with an accuracy of 0.03 mm for movement along the z-axis. Figure 2.2 (b) depicts the coordinate system based on burner geometry used in this study.

The pinhole was centered along the centerline of the burner before each test using the three translation stages and a cone shaped object that fits into the throat of fuel tube that has a centrally located needle (Figure 2.5) on which to align the sample port. It should be noted that pinholes should always be as small as possible so that a better special resolution could be achieved; however, there are conditions that prevents the use of very small pinholes. The foremost detriment in choosing very small pinholes is the clogging of the pinhole due to soot deposition which could affect the measurements. In our study it was found that pinholes smaller than 0.2 mm resulted in complete clogging of the pinhole by soot particles in a time less than the duration of a measurement with the particle measurement suite. For instance, in heights above burner

(HAB) below 39 mm and above 55 mm the concentration and size of the particles are low enough to provide sampling with a 0.2 mm pinhole. Other HABs were sampled with a probe that has a 0.3 mm pinhole. It should be noted that due to gradual clogging, the pinhole is needed to be cleaned by a fine wire periodically.
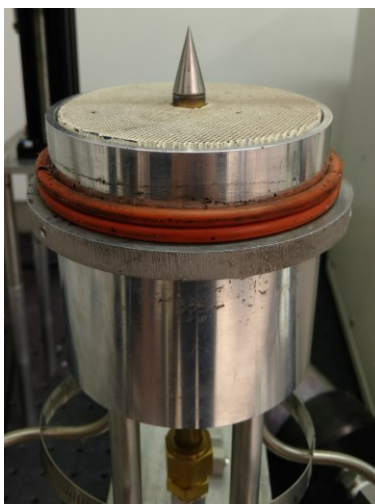
Figure 2.5. Cone shaped central indicator used for alignment of the pinhole of the sample probe

The diluent nitrogen that flows through the sampling probe in this study was set at 17.5 SLPM with a mass flow controller (Omega, Model FMA-5540). As illustrated in Figure 2.1, to establish a negative pressure throughout the sampling system the downstream of the probe tube was attached to a vacuum pump (GAST, Model DAA-P501). A make-up nitrogen flow was added to the main sampling line prior to the vacuum pump connection to control the extraction flow through the pinhole (see Figure 2.1). The make-up nitrogen flow was controlled by a mass flow controller (Omega, Model FMA-2608A). By the help of an eductor pump (AIR-VAC, Model AVR093H) a fraction of sample was drawn from the main sampling line through a branch placed between the pinhole and make-up nitrogen. The portion of sample that was drawn from the

sampling line was subsequently directed to a gas analyzer (Li-Cor 840) and particle measurement suite. The eductor pump is a Venturi tube in which a flow of nitrogen (10 SLPM) controlled by an mass flow controller (Omega, Model FMA-775-V) passes through its inlet and generates vacuum which is used for sample extraction from the main sampling line.

To maintain a constant dilution ratio the concentration of CO_2 was monitored by the gas analyzer (Li-Cor 840), and a PID controller acquired the CO_2 concentration readings and manipulated the make-up flow rate such that the concentration of CO_2 remained at a constant level. By measuring the gauge pressure at the vicinity of the pinhole it could be verified whether samples were extracted through the pinhole or not. For measuring the gauge pressure at the pinhole a 0.8 mm OD stainless steel tube was inserted inside the sampling probe from the upstream side of the probe and connected to a manometer. It should be noted that due to sudden changes of pressure that could occur during diluted sampling a monometer is used instead of a pressure transducer.

2.2.2.2   Undiluted Sampling System

Particles extracted from the flame by the dilution sampling systems are diluted several thousand times; however, if used alone this system of sampling cannot provide any insightful information on the magnitude of dilution and hence the particle concentration where sampled. One of the methods that can be used to evaluating the amount of dilution is to measure the mole faction of a gas species in both diluted and undiluted conditions. Therefore, a sampling system was required to extract samples without diluting them. Figure 2.6 shows the undiluted sampling system.
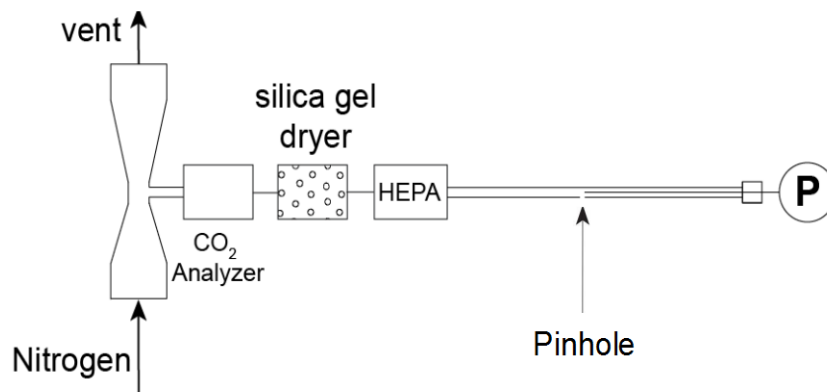
Figure 2.6. Schematic of the undiluted sampling system (Kazemimanesh et al. 2016).

Some major changes were applied to the diluted sampling set-up to alter it into an undiluted sampling system. Instead of using a pump for extracting particles through the probe, the downstream sampling line was connected to the throat of an aluminum Venturi tube with inlet and throat diameters of 10 mm and 5 mm, respectively. The other end of the sampling line was capped. The Venturi acted as a pump when nitrogen flow passed through it and dropped the pressure at the throat. The reason that a Venturi tube was used instead of the diaphragm pump is that the diaphragm pump created a disturbance in the flow which resulted in a fluctuation of pressure and the suction created by the pump was higher than what was needed; however, the suction created by the Venturi tube did not impose any disturbances on the pressure and a small amount of suction was created by the Venturi. Since the sampling line is attached to the Venturi throat the pressure drop would lead to a suction of sample flow through the pinhole of the probe and the only flow through the probe would be the flow of sample extracted from the flame.

As demonstrated in Figure 2.6, between the sampling probe and the Venturi tube a HEPA filter, a tube filled with silica gel, and a CO2 analyzer (Gas Sensing Solutions, Model COZIR-20%)

were placed. The mole faction of CO_2 was measured at different ΔP across the pinhole with a pressure transducer (Cole-Parmer, Model RK-98073-04). At low pressure differences (~50 Pa) the concentration of CO_2 in a given location of the flame became independent of pressure difference and is the representative concentration of CO_2 at that location. If the pressure difference is very small, the extracted sample flow rate decreases and it takes a longer sampling time for the instrument to reach to a stable concentration of CO_2. The longer sampling time could result in clogging of the pinhole prior to reaching a stable concentration for CO_2.

There are few remarks that need to be addressed about the undiluted sampling. Firstly, it should be noted that the time window required for the gas analyzer to measure the concentration of CO_2 is quite long (more than 3 min). Neither the 0.2 mm nor the 0.3 mm pinholes can remain unclogged after about 2 min therefore the concentration of CO_2 in the undiluted condition was measured with a 0.5 mm pinhole that could provide enough time for the CO_2 gas analyzer to measure stable data. Additionally, it should be noted that prior to the gas analyzer a diffusion dryer was placed; hence, the concentration of CO_2 measured in the undiluted condition is the concentration of CO_2 without H_2O. The main reason for the use of diffusion dryer is the fact that the gas analyzer could not be operated at high humidity. To include the concentration of H_2O and have an estimate of the real concentration of CO_2 the results acquired from our measurements were compared to the results of another experiment conducted on a very similar geometry and fuel flow condition (Mitchell 1975). The results from Mitchell (1975) shows that when burning methane the concentration of H_2O is approximately two times the concentration of CO_2 at different HABs. Based on the trend observed in Mitchell's work it was decided to consider the concentration of CO_2 to be half the concentration of H_2O and the results was corrected accordingly.

2.2.2.3   Dilution Ratio Measurements

Since the particle size distribution measured by the aerosol instrument suite is based on a sample that is diluted, it is necessary to know exactly how dilute the samples are and scale up the results accordingly. The exact amount of dilution can be acquired by introducing a parameter named the dilution ratio. Assuming similar composition of sample gas in diluted and undiluted cases, the overall dilution ratio (*DR*) is defined as

$$DR = \frac{X_{CO_2, \text{undiluted}}}{X_{CO_2, \text{diluted}}} \tag{2.1}$$

where $X_{CO_2, \text{undiluted}}$ and $X_{CO_2, \text{diluted}}$ are the mole fraction of CO_2 in the undiluted and diluted samples at the same pressure and temperature, respectively. Particle size distribution results must be multiplied by the dilution ratio for each flame location to correct the measurement to the sample location condition.

2.2.3   Particle Measurement Suite

The size distribution of particles was measured using a scanning mobility particle sizer (SMPS; TSI Inc., Model 3080), which consisted of a nano differential mobility analyzer (nano-DMA; TSI Inc., Model 3085) for particle sizing and a condensation particle counter (CPC; TSI Inc., Model 3776) for particle counting. The aerosol and sheath air flow rates were set at 1.5 L/min and 15 L/min, respectively, for a full-width half-maximum resolution of one tenth the mobility set point and provided a particle sizing range of 2-60 nm. Typically, a particle size distribution was obtained from a 40 s scan after ~10-min initial waiting time for the flame to stabilize. The particles were drawn into the nano-DMA via silicone conductive tubing by the CPC pump. In

non-conductive tubing static charges can be imposed in regions of the tube which can attract particles with opposite charges and lead to particle loss; therefore, it is always necessary to employ conductive tubing for transport of aerosol samples.

2.2.4   **Thermophoretic Sampling and Transmission Electron Microscopy**

To analyze the morphology of nano-particles with transmission electron microscopy (TEM) particles were sampled on TEM grids. Thermophoretic sampling is usually employed for collecting soot particles onto TEM grids (Zhao et al. 2007; Abid et al. 2008; Kholghy et al. 2013). Thermophoresis is a net force acting on particles when they are exposed to a thermal gradient. Thermophoresis is exerted on particles in the same direction as the temperature is decreasing (Hinds 1999), thus particles move toward colder surfaces. This phenomenon is the basis for collecting soot particles on TEM grids. In this study a thermophoretic sampler (TPS Mark III) was provided by the University of British Colombia. The thermophoretic sampler drew a portion of diluted sample prior to the particle measure suite. Figure 2.1 shows the thermophoretic sampler with the diluted sampling system and aerosol measurement suite. The thermophoretic sampler increases the temperature of the sample flow and directs the flow to a stage where the TEM grid is located at room temperature and as a result of thermophoresis the heated particles intercept the cold grid. The TEM grids used for collecting samples were ultra-thin carbon film supported by a lacy carbon film on a 400 mesh copper grid (Ted Pella Product No. 01824). The morphology of soot particles was investigated by analyzing TEM grids with a JEOL 2100 transmission electron microscope. The microscope was used for both low resolution and high resolution imaging.

2.2.5   Temperature Measurement System and Temperature Correction

2.2.5.1   Thermocouple Holder

The temperature at different radial and axial positions of the reacting flow was measured with a type R thermocouple (Pt/13%Rh-Pt, Omega). The wire diameter was 75 μm and the junction size was approximately 190 μm (same order of magnitude as the pin hole for sampling). The thermocouple was mounted on a holder that was similar to a thermocouple holder described in several studies (Cundy et al. 1986; McEnally et al. 1997; Abid 2009). Figure 2.7 shows an image of the thermocouple mount.
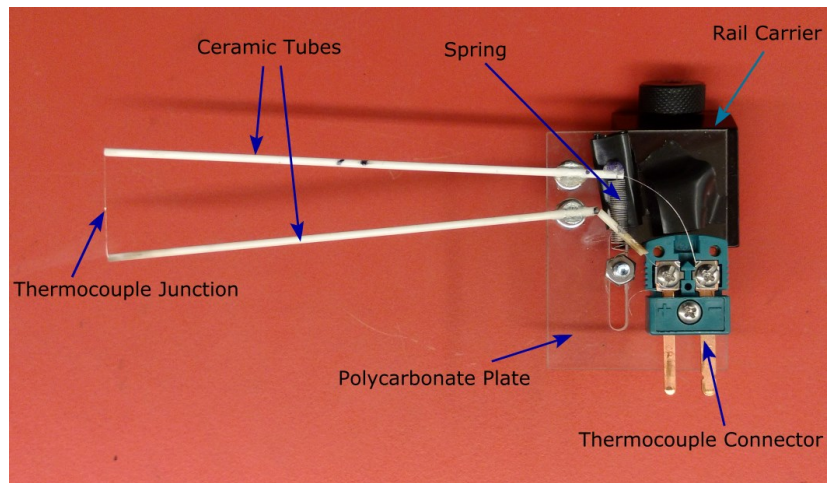
Figure 2.7. The thermocouple mount used in temperature measurement system.

The thermocouple mount comprises of two ceramic tubes with an outer diameter of 1.6 mm and lengths of 100 mm and 110 mm. The ceramic tubes were attached to the head of screws as mentioned in (McEnally et al. 1997) and one of the screws was tightened to a polycarbonate plate while the other screw was relatively loose to allow the screw to pivot. The ceramic tubes act as a support for the thermocouple wire. The legs of the thermocouple wire are attached to a thermocouple connector on the bicarbonate plate while a portion of the thermocouple wire

between the ceramic tubes was exposed to the air. The thermocouple junction is located at the middle of the exposed portion of the thermocouple wire. A spring was connected to the pivoting ceramic tube to keep the exposed portion of the thermocouple stretched. The main reason for using the spring on the pivoting tube was to keep the exposed thermocouple under tension in high temperatures and prevents sagging of the wire due to expansion.

Figure 2.8 shows a scheme of the temperature measurement system. The polycarbonate plate was attached to a dovetail rail carrier (Thorlabs RC1). The rail carrier was mounted on an optical rail (Thorlabs RLA0600) which allowed the thermocouple holder to be displaced along the radial direction of the burner. One end of the optical rail was attached to a stepper motor driven traverse with a straight line accuracy of 0.03 mm that would allow the thermocouple to be placed at different axial positions. On the other end of the optical rail a stopper with a switch was placed. Once the dovetail rail carrier reaches the stopper the switch is activated and data acquisition system starts to collect the temperature measured by the thermocouple.
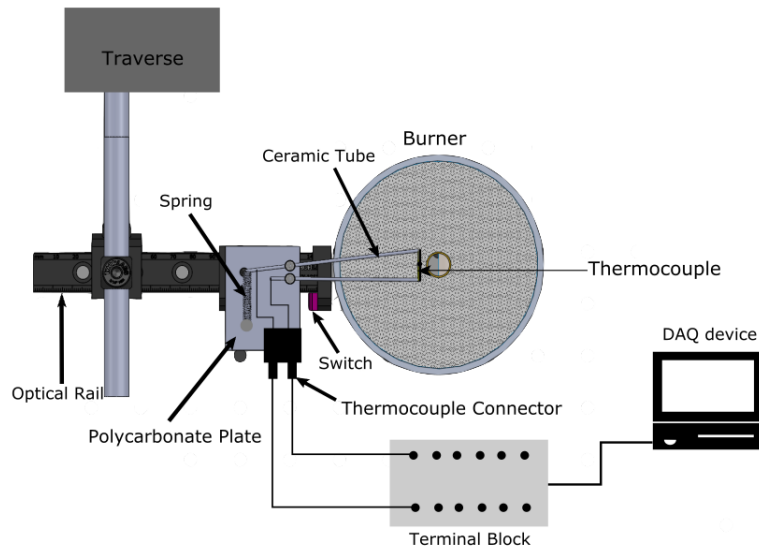
Figure 2.8. Schematic of the temperature measurement system.

2.2.5.2   Temperature Measurements

As mentioned earlier, the temperature of the flame was measured at various radial and axial locations in the reacting flow. The thermocouple was inserted swiftly in different regions of the flow and as soon as the thermocouple reached the stop position indicated by the switch, the data acquisition started and lasted for about two seconds with a sampling rate of 100 Hz. This technique of temperature measurement is known as the rapid thermocouple insertion technique (McEnally et al. 1997). Long exposure (more than 7 seconds) of thermocouple wire inside the flame results in failure of thermocouple wires. Additionally, the soot deposition on the thermocouple changes the emissivity of the junction and result in a drop in temperature

measurements. Wire failure and soot deposition on the thermocouple are the main reasons for employing rapid thermocouple insertion techniques.

Figure 2.9 shows temperature measurements from regions of the flow where high and low concentrations of soot exist. In locations with low concentration of soot particles, the data showed a swift increase in temperature followed by a plateau. This trend could not be seen in other locations with large concentrations of soot particles. The results from sooty locations showed a swift increase in temperature followed by a peak and then a drastic decrease in the measurement. These trends were also observed in several other studies (McEnally et al. 1997; Kholghy 2012; Abid 2009). McEnally et al. (1997) stated that results obtained by the rapid insertion technique have several stages. The first stage is the transient response stage which starts from the moment sampling commences until it reaches either a plateau or a peak. For lightly sooting locations the temperature measured after the transient time is more-or-less constant. For heavy sooting locations the next stage is the variable emissivity stage (and increased surface area) which results in a decrease in temperature after the transition stage.

The representative temperature for each location depends on whether the desired location is highly sooty or not. Kholghy (2012) considered the magnitude of the plateau as the representative temperature in lightly sooty regions and the magnitude of peak as the representative temperature in heavily sooty regions.
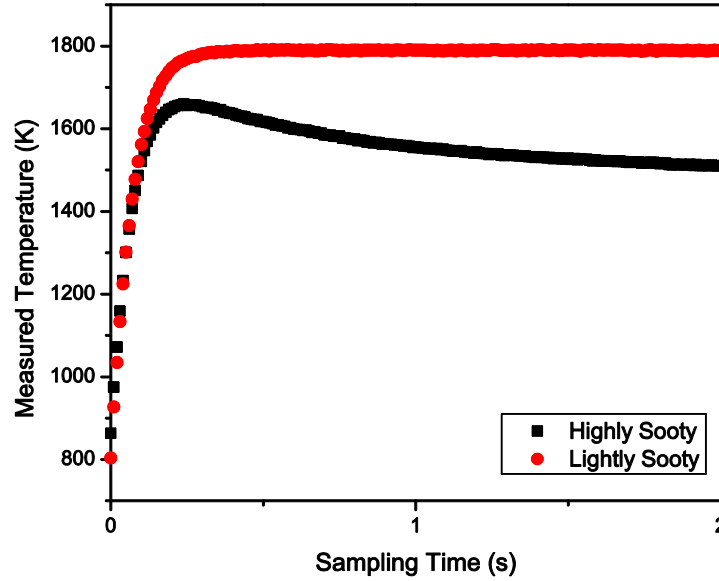
Figure 2.9. Effect of soot deposition on thermocouple measurements

To determine if the thermocouple was in a highly sooting or lightly sooting region, the measured temperatures from $t = 0.75$ s to $t = 2$ s were fitted by a first order polynomial. It was assumed that if the polynomial fit has a slope larger than 20 K/s the measured data was in a highly sooting region and the maximum measured temperature was considered to be the gas temperature.

For lightly sooting regions the gas temperature was assumed to be the average of measured data from 5τ to 7τ, where τ is the time constant assuming the measured temperature during the sampling time is a step response function that can be approximated by the following equation:

$$T = A\left(1 - e^{-\frac{t}{\tau}}\right) + B \tag{2.2}$$

where B is the value of temperature measured by the thermocouple at $t = 0$ s and τ is the time constant. In Eq. 2.2, A is equal to

$$A = C - B \tag{2.3}$$

where C is the mean value of the measured temperatures from $t = 0.5$ s to $t = 2$ s. It should be noted that at $t = \tau$ we have:

$$T(\tau = t) = A(1 - e^{-1}) + B \tag{2.4}$$

The range of the times constants measured was between 0.1 s to 0.25 s which is quite similar to the time response of thermocouples measured by McEnally et al. (1997).

2.2.5.3   Temperature Correction

It should be noted that the desired temperature for this study is the gas temperature and not the collected temperature from thermocouple measurements. It is required to apply corrections to the data measured by the thermocouple to obtain the temperature of the gas.

To understand the relation between gas temperature and thermocouple temperature, the energy balance for the thermocouple should be obtained. Equation 2.5 is the energy balance equation for a thermocouple suggested by Shaddix (1999):

$$\dot{Q}_{rad} + \dot{Q}_{conv} + \dot{Q}_{cond} + \dot{Q}_{cat} = \rho_{th} c_p V_{th} \frac{dT_{th}}{dt} \tag{2.5}$$

where $\dot{Q}_{rad}$ is the radiation heat transfer, $\dot{Q}_{conv}$ is the convective heat transfer, $\dot{Q}_{cond}$ is the conductive heat transfer and $\dot{Q}_{cat}$ is the heat transfer due to catalytic reactions. T_{th} is the thermocouple temperature, c_p is the specific heat of thermocouple, ρ_{th} and V_{th} are the density and volume of the thermocouple respectively.

Thermal conductivity can cause heat loss in the thermocouple due the conductive heat transfer from the junction and other hot parts of the wire to cooler regions. It was suggested by Heitor and Moreira (1993) that the heat loss due to conduction is insignificant if the length to diameter ratio of thermocouple is more than 200. In our study the length to diameter ratio is more than 200; therefore, in the correction analysis it was assumed that the heat transfer due to conduction is negligible.

The catalytic reactions could occur between radicals at the surface of the thermocouple junction (Shaddix 1999). Characterizing the effect of catalysis on thermocouple outputs is a relatively difficult task. Coating the surface of the thermocouple with a nonreactive material such as silica can mitigate the effect of catalytic reactions and was applied in several studies (Abid 2009; Katsuki et al. 1987). However, there are other studies that did not apply coatings on the thermocouple surface (Ballantyne & Moss 1977; McEnally et al. 1997; Saffaripour et al. 2011; Kholghy et al. 2015). Ballantyne and Moss (1977) measured the temperature of a turbulent methane diffusion flame claimed that the heat loss due to catalysis would contribute to about 20 K in temperature measurements. On the other hand, McEnally et al. (1997) measured the temperature of a laminar methane diffusion flame using rapid insertion of an uncoated R-type thermocouple and mentioned that the catalysis effect was negligible in diffusion fames.

By neglecting the heat losses due to conduction and catalytic reactions and considering steady state condition, Eqn. 2.5 becomes:

$$\dot{Q}_{rad} + \dot{Q}_{conv} = 0 \qquad\qquad (2.6)$$

In this study, it was assumed that the thermocouple has a diffuse grey emitting surface and is surrounded by an isothermal diffuse grey wall (Shaddix 1999). Additionally, the surface area of the wall is much greater than the surface area of the thermocouple. With these assumptions Eqn. 2.6 becomes:

$$\varepsilon\sigma A(T_{th}^4 - T_W^4) - Ah(T_g - T_{th}) = 0 \qquad (2.7)$$

By rearranging Eqn. 2.7 the gas temperature is:

$$T_g = T_{th} + \frac{\varepsilon\sigma}{h}(T_{th}^4 - T_W^4) \qquad (2.8)$$

Rewriting Eqn. 2.8 based on the Nusselt number (Nu) results in:

$$T_g = T_{th} + \frac{\varepsilon\sigma}{Nu}(T_{th}^4 - T_W^4)\frac{d}{k} \qquad (2.9)$$

where d is the thermocouple junction diameter and k is the thermal conductivity.

There are several models that describe the convective heat transfer. These models are based on different empirical correlations of Nusselt number. In the current study it was assumed that the junction has a spherical geometry. For forced convection heat transfer around a sphere Whitaker correlation (Whitaker 1972) was used for obtaining the Nusselt number:

$$Nu = 2 + (0.4Re^{\frac{1}{2}} + 0.06Re^{\frac{2}{3}})Pr^{0.4}(\frac{\mu_g}{\mu_j}) \qquad (2.10)$$

where Re is the Reynolds Number and Pr is the Pranadtl number and μ_g and μ_j are the viscosity of gas and thermocouple junction respectively. Inserting Eqn. 2.10 into Eqn. 2.9 lead to the following Eqn. for gas temperature:

$$T_g = T_{th} + \frac{\varepsilon\sigma}{2 + (0.4Re^{\frac{1}{2}} + 0.06Re^{\frac{2}{3}})Pr^{0.4}(\frac{\mu_g}{\mu_j})}(T_{th}^4 - T_W^4)\frac{d}{k} \qquad (2.11)$$

The junction diameters in the thermocouples were two to three times the size of wire diameter. In our analysis it was assumed that the thermocouple junction has a diameter of 190 ± 37 μm (the size of the junction is estimated based on the information provided by the manufacturer). It should be noted that in Eqn. 2.11 Re, Pr and k are function of gas composition and temperature. Thus, to derive these parameters the gas composition of flame must be known. The gas composition and velocity were obtained from a study conducted by Mitchell (1975) on a relatively similar burner geometry with similar fuel flow condition. For simplicity the approximated gas composition consisted of only six species: CO_2, H_2O, CO, H_2, CH_4 and N_2. Viscosity, density and thermal conductivity were calculated using Cantera software.

Another important temperature depending variable in Eqn. 2.11 is emissivity. Numerous studies (McEnally et al. 1997; Saffaripour et al. 2011; Kholghy 2012) that conducted thermocouple measurements with type-R thermocouples and rapid insertion techniques used the emissivity calculated by Bradley and Entwistle (1961). In their study, Bradley and Entwistle measured the

emissivity of platinum and platinum/10% rhodium in a range of temperatures. Although Bradley and Entwistle (1961) measurements are for type-S thermocouples, since the material compositions of type-S thermocouple is similar to type-R thermocouple (platinum and platinum/13% rhodium), research groups working with type-R thermocouple also used the results of Bradley and Entwistle. In our study we also estimated the emissivity of thermocouple based on Bradley and Entwistle measurements.

2.2.6   NaCl Injection System

One of the main objectives of this project is to investigate the effect of NaCl on soot formation. Therefore, it is essential to add another component to the experimental set-up for introducing the soot particles into the flame. The salt crystals are produced by atomizing a solution of NaCl (25 % by mass) with a nebulizer (Aerogen Solo). The atomized droplets of NaCl solution are passed through a diffusion dryer to remove the water and introduced to the fuel line. Hence, the vast majority of additive that is injected into the flame is crystalized NaCl.   The NaCl injection system is shown in Figure 2.1. By adding a relay to the nebulizer controller the rate of NaCl droplets production in the nebulizer could be manipulated (Park et al. 2015). Figure 2.10 shows a picture of the flame when the salt particles are injected into the flame. It can be seen that the injection of salt particles changes the color of the flame and creates a halo region around the flame. Based on the size distribution of NaCl particles at the burner outlet and density of salt particles the mass concentration of particles inserted into the flame was calculated to be 49 ng/cm^3 which is explained in more detail in Appendix B.

Figure 2.10. Laminar co-flow methane diffusion flame with NaCl additive.

Chapter 3

Results and Discussion

In this chapter all the results obtained from the experiments are delineated. Firstly, the results from temperature measurements and temperature profiles of the flame in both the pure methane flame and the flame dope with NaCl are included which is followed by the effect of the sampling probe on the temperature profile along the central axis of the flame. Secondly, the evolution of particle size distributions along the centerline of the flow was included for both cases of the pure methane flame and the methane flame doped with NaCl. Thirdly, the effect of NaCl on the evolution of soot particle size distribution is discussed.

3.1 Temperature Profiles of the Methane Diffusion Flame and the Methane Flame with NaCl Additives

The process of nano-particle formation is significantly affected by temperature. An understanding of nano-particle formation in a laminar diffusion flame cannot be achieved unless temperature is measured.

The temperature profiles from the centerline to a radial position of 8 mm for selected heights above burner (HAB) from 1 mm to 60 mm were measured for cases of the pure methane flame and the methane flame doped with 49 ng/cm^3 of NaCl additive. The temperature profile at different HABs along the centerline of the flame is demonstrated in Figure 3.1. Temperature at each location was measured at least four times and the average of measured temperatures are illustrated in Figure 3.1 in which all the temperatures were corrected for radiation heat transfer

(see section 2.2.5.3 for details). The maximum uncertainty of the measured temperatures was ~± 40 K (see Appendix C). Based on the results the temperatures are quite similar for both cases of the pure methane flame and the methane flame with NaCl additives with the minimum and maximum variations being 13 K and 40 K, respectively. As shown in Appendix D the small difference in flame temperature between the two cases is in agreement with theoretical adiabatic flame temperatures. As the introduction of NaCl particles into the flame does not affect the flame temperature significantly, it can be inferred that soot particles in both flames experience similar temperature conditions.
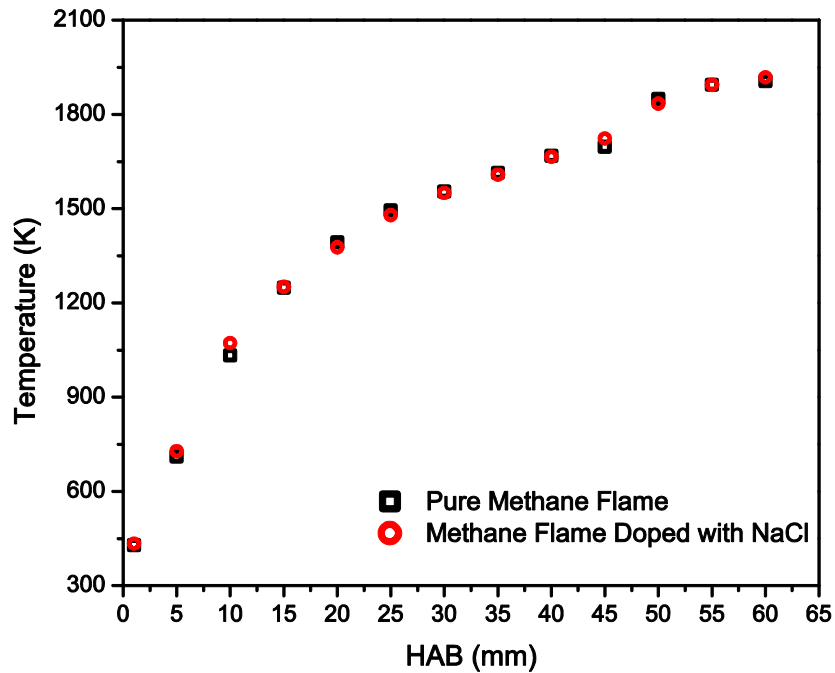
Figure 3.1. Axial temperature profile of pure methane flame and methane flame doped with NaCl.

Figure 3.2 is a contour plot of measured flame temperatures for the case the methane flame doped with NaCl particles and it is based on the radial temperatures acquired from different HABs. The black and red lines in the contour demonstrate the boundaries of melting and boiling

42

temperature of NaCl at one atmosphere, respectively. The dashed line is an approximate location

of the visible flame surface.
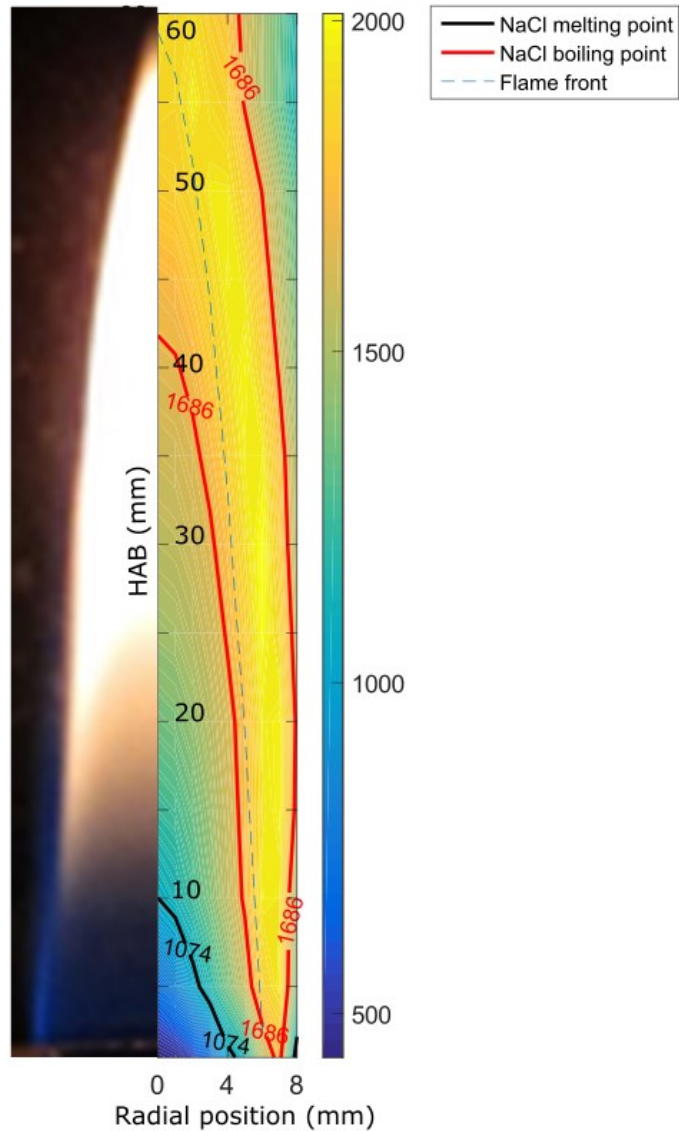
Figure 3.2. Picture of flame and contour of flame temperature (K) in case of the methane flame doped with NaCl particles

3.2   **Effect of Sampling Probe on Flame Temperature at Central Axis**

The insertion of the sample probe into the flame disturbs the temperature profile and will reduce

the temperature at the vicinity of the sampling probe; therefore, it is necessary to investigate the

effect of probe insertion on the flame temperature as that could potentially affect the formation of particles that are being sampled. This investigation was done by inserting the sampling probe at several locations, and measuring the temperature along the stagnation streamline from 0.5 mm to 10 mm upstream of the location of the probe. Figure 3.3 demonstrates the temperature profiles when the probe is inserted at different locations and when the probe is not in the flame. The blue dashed lines are locations where the probe was inserted while the temperatures for HABs below these locations were measured.

The results show that the insertion of the probe affects the temperature of points that are located approximately within 3 mm of the probe locations. The temperature drop within the last 3 mm below the probe is significant and is as high as ~600 K. As mentioned earlier the process of soot formation is related to the temperature and a significant temperature drop due to probe insertion could slow down reactions within the last 3 mm before the probe. The temperature trend is similar to the results obtained by Zhao et al. (2003b) which reported a decrease in local flame temperature in a region 3 mm below the probe. They argued that the local temperature drop is an intrinsic disadvantage of probe sampling which result in a decrease of chemical reactions that affects the soot formation. Abid et. al (2008) used probe sampling with an SMPS and thermocouple densitometery (which does not disturb the flame significantly) and found that soot volume fractions were similar if the HAB of the SMPS results were shifted 3.5 mm downward; presumably because the probe slows reactions near the probe.
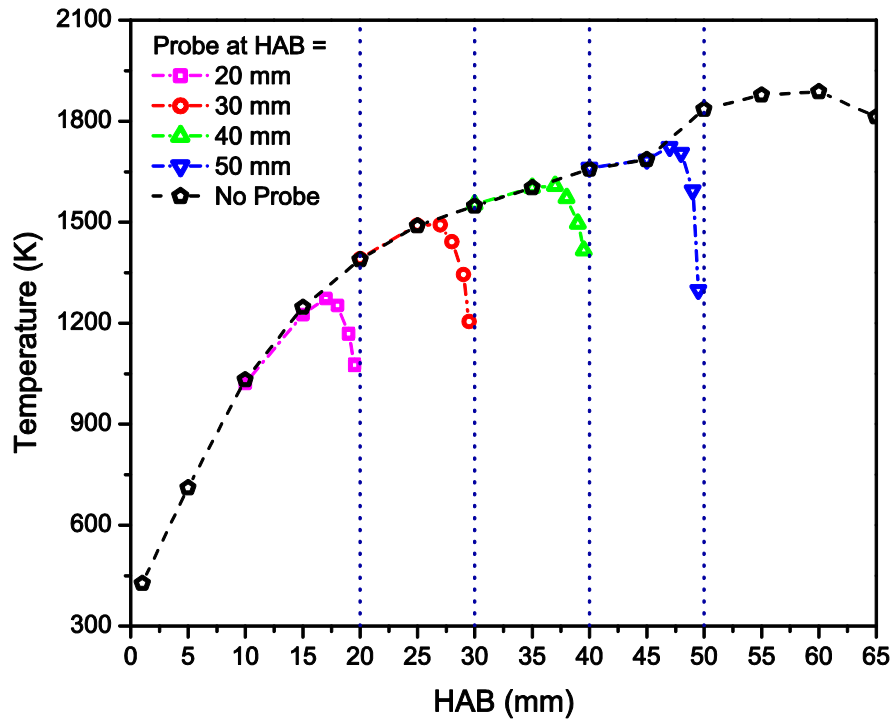
Figure 3.3. Temperature measured at the central axis for pure methane flame with and without probe. The blue dashed lines are the location where probe was inserted.

3.3 Particle Size Distribution Measurements

3.3.1 Effect of Dilution on Particle Size Distribution

Particle losses or particle-particle coagulation changes the particle size distribution as the aerosol sample flows through the sampling probe and sampling system. Significant particle coagulation (caused by high concentrations of particles) causes larger particles to form and reduces the total number concentration of the aerosol. The rate of particle coagulation is dependent on the concentration of particles (Hinds 1999) and the coagulation rate can be reduced by immediately diluting the aerosol once it enters the sampling probe. Once a critical dilution ratio is reached (*i.e.* the particle number concentration is sufficiently low), the effect of coagulation is negligible

and the measured particle size distribution multiplied by the dilution ratio will be equal to the particle size distribution entering the sampling probe. Zhao et al. (2003b) and Camacho et al. (2015) refined this probe sampling technique to achieve this critical dilution ratio for premixed flames and the same path was followed in a study conducted on a Santoro burner by Kazemimanesh et al. (2016). Similar to the method employed by Kazemimanesh et al. (2016), a wide range of dilution ratios were used at each height to investigate its effect on the measured particle size distribution (PSD).

Figure 3.4 shows the variation in the dilution-corrected particle size distributions (*i.e.* the measured size distribution multiplied by the dilution ratio) for HAB=38 mm when the dilution ratio was changed by more than an order of magnitude from 820 to 13,400. With low dilution ratios, the PSD was unimodal and no particles smaller than 3 nm were detected. As the dilution ratio increases the distribution appears to become bi-modal, with one mode with a median diameter greater than 3 nm and, presumably, one mode of greater number concentration with a median diameter below 2 nm (which is below the lower detection limit of the nano-DMA), of which only the tail is observed. Figure 3.4 shows that at dilution ratios greater than ~ 6300 the PSDs become approximately independent of dilution ratio and converge to a specific PSD.
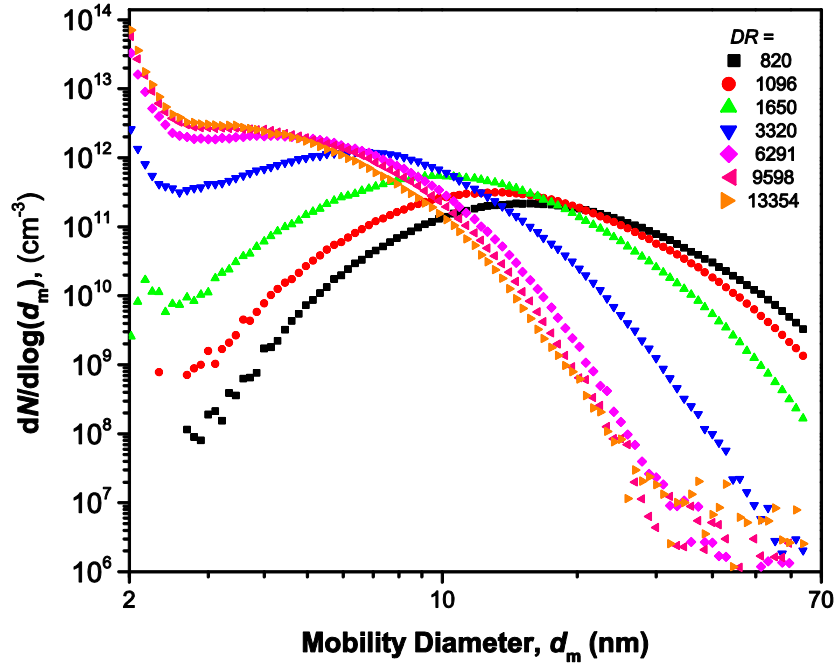
Figure 3.4. Variation of corrected particle size distribution as a function of dilution ratio for HAB=38 mm.

Figure 3.5 shows the count median diameter of the PSDs in Figure 3.4 (or count median diameter of the second (larger) mode in the case of the bi-modal distributions) as a function of dilution ratio. The median diameters were calculated based on a bimodal lognormal fit of the measured PSD. Once the dilution ratio reached the critical value of ~6,300 for this specific HAB, the particle median diameter remained approximately constant. Zhao et al. (2003b) and Camacho et al. (2015) using premixed flames, also found that once a critical dilution ratio was reached the median diameter of the PSD became independent of dilution ratio.
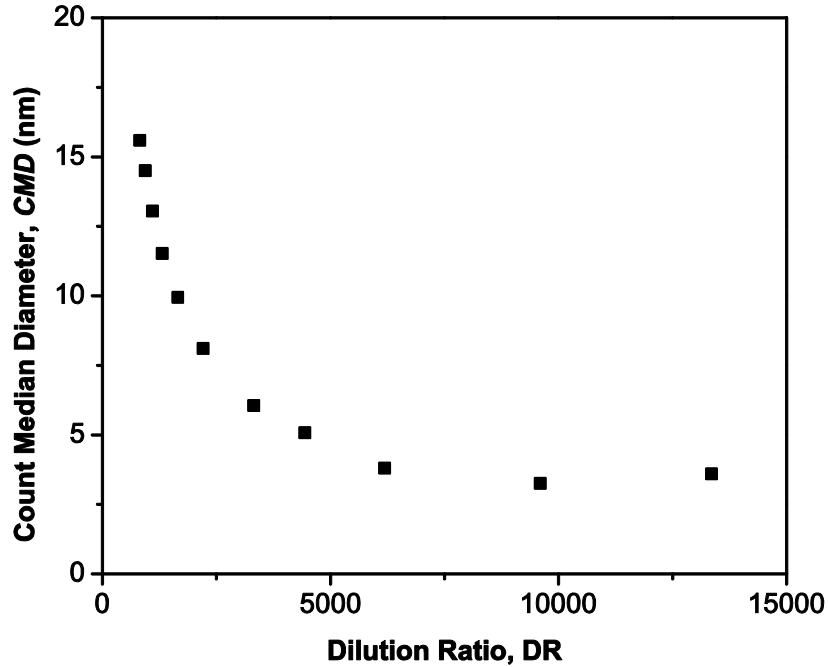
Figure 3.5. Variation of particle median diameter as a function of dilution ratio for HAB=38 mm.

In our study the effect of dilution ratio on the particle size distribution was investigated for PSDs acquired at each sample location. For each HAB the PSDs were measured at 3 or 4 different dilution ratios and the results presented in the following sections are PSDs in which the corrected size distribution is approximately independent of dilution ratio. For HABs above 48 mm significant increases in dilution ratio led to an increase in size of particles instead of reducing the overall size which was seen in heights below 49 mm. This phenomena was observed by Camacho et al. (2015), presumably because extremely high dilution leads low velocities through the pin hole resulting in higher particle losses and coagulation rates. Thus a high dilution ratio does not always result in a better measurement so for each height a range of dilution ratios was tested.

3.3.2 Evolution of Nano-Particles in the Pure Methane Flame

Particle size distributions for different heights above the burner along the centerline of the flame were measured. The purpose of this part of the experiment was to create a detailed understanding of nanoparticle size and number concentration along the central axis of the laminar diffusion flame to investigate how the particles evolve. Particle size distribution results are useful for theorizing about the processes of soot formation that take place at different HABs of the diffusion flame; however, SMPS results do not provide any information of the structure and shape of particles. Transmission electron microscopy (TEM) is one of the tools that can be used to obtain information on shape and structure of particles. To have a better understanding of the evolution of nano-particle formation and growth, TEM images from different HABs are also included in this section.

For the sake of clarity, the particle size distributions are broken into five plots to better represent the trends in particle evolution. Figure 3.6 shows the particle size distribution from HAB=30 mm to HAB=38 mm along with a TEM image of particles at HAB=36 mm.

(a)   (b)
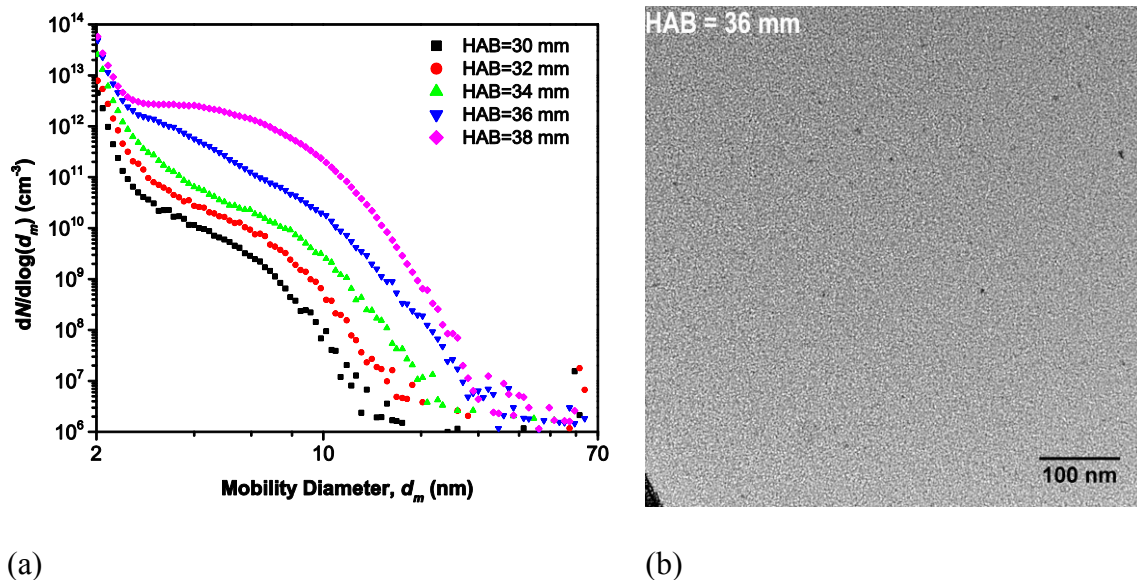
Figure 3.6. (a) Particle size distributions for HAB=30–38 mm in pure methane flame. (b) TEM image from HAB=36 mm

Below HAB=30 mm, the SMPS could not detect any particles. At the onset of particle nucleation at the height of 30 mm, a small fraction of the tail of the PSD could be detected which mostly consisted of nanoparticles smaller than 3 nm. As HAB increased, particles with mobility diameter greater than 3 nm grew in size and concentration, which led to an observable bi-modal modal distribution at HAB=38 mm. Herein, the smaller mode will be called the inception mode and the larger mode will be called Mode I. The TEM results from HAB=36 mm (Figure 3.6b) suggest that the particles (the small dark circular shapes in the figure) from HAB=36 mm are individual non-aggregate soot particles. Figure 3.7 is a high resolution TEM (HRTEM) image from a particle at HAB=36 mm. As it can be seen from Figure 3.7, the particle is difficult to observe as there is not a significant contrast between the particle and the background. It was a difficult task to take pictures with high resolution from particles at HAB=36 mm since the particles were sensitive to the microscope beam and hard to detect.
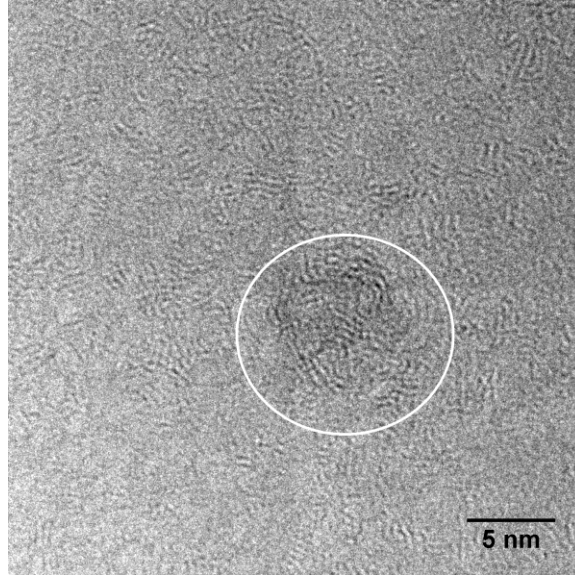
Figure 3.7. HRTEM image of a particle at HAB=36 mm

Figure 3.8 shows the particle size distribution from HAB=39 mm to HAB=43 mm and a TEM image from HAB=40 mm. For HAB=39 mm to 41 mm (Figure 3.7a), Mode I increases in both size and number while the inception mode remains approximately constant in magnitude. At HAB=42 mm particles with mobility diameter greater than 10 nm begin to form another mode which will be called Mode II (in Figure 3.8 this mode is located at ~30 nm).
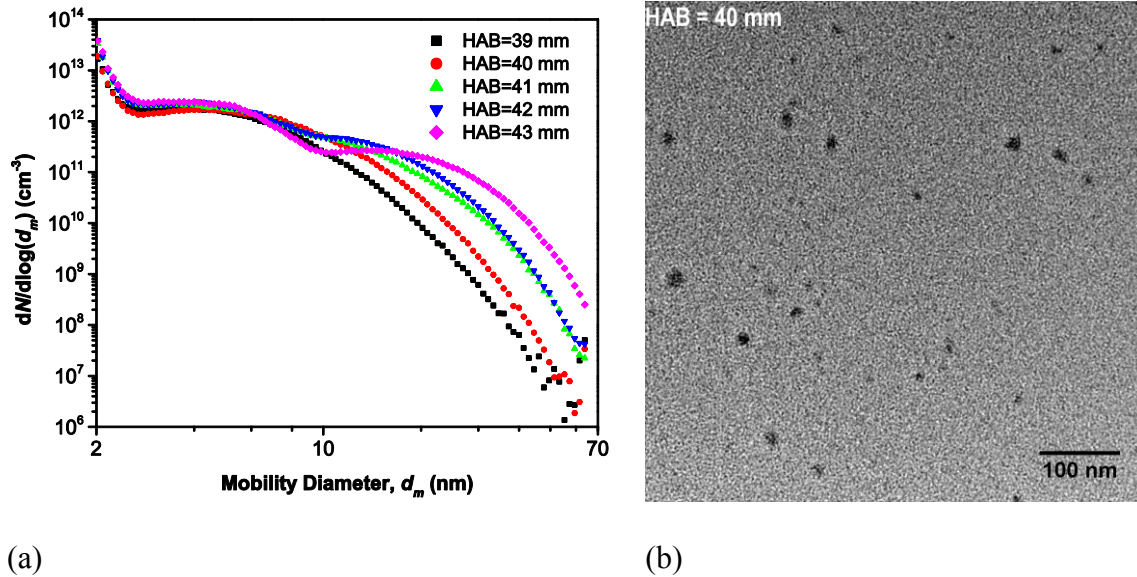
Figure 3.8. (a) Particle size distributions for HAB=39–43 mm in pure methane flame. (b) TEM image from HAB=40 mm.

TEM images from HAB=40 mm shows that particles appear to have a non-aggregated structure while their size have grown compared to particles at HAB=36 mm. Figure 3.9 shows HRTEM images of particles from HAB=40 mm and HAB=41 mm. Particles from HAB=40 mm and 41 mm where less sensitive to the microscope beam and were easier to detect. The HRTEM images show that the soot particles consist of single or multiple core-shell structures. The core-shell structure of soot particles has been reported in other studies (Chen & Dobbins 2000; Botero et al. 2016; An et al. 2016). It was mentioned that the core has an amorphous structure with no particular graphite layer while the shell consists of graphite microcrystalline structure (An et al. 2016).
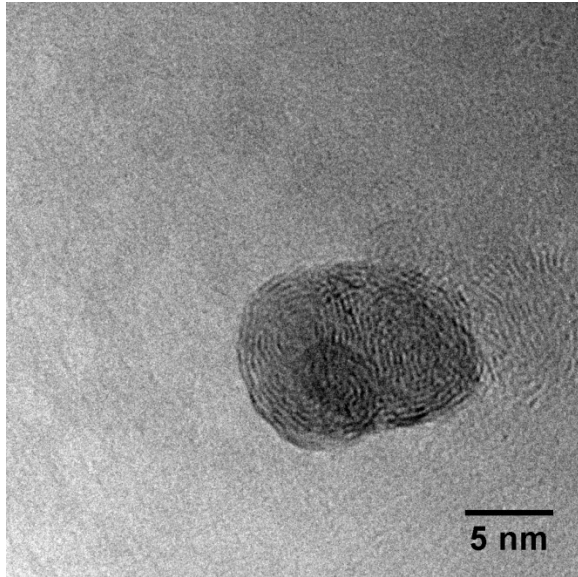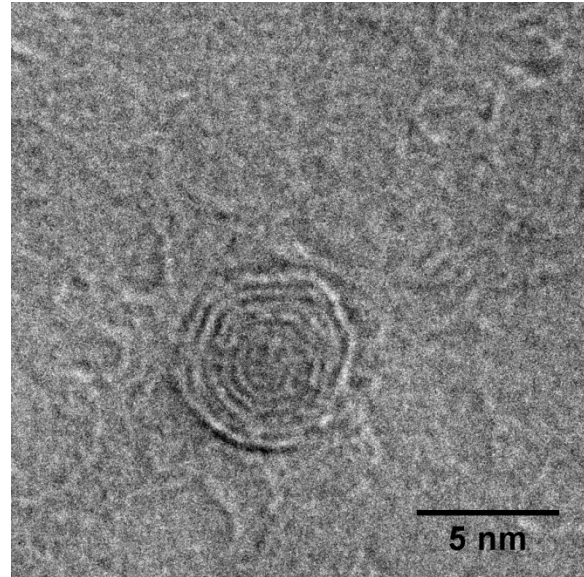
(a)   (b)

Figure 3.9. (a) HTEM image from HAB=40 mm. (b) HRTEM image form HAB=41 mm

Figure 3.10 shows the particle size distribution from HAB=44 mm to HAB=48 mm and a TEM image from HAB=45 mm. Here, the median particle size in Mode II grew larger while the particles in Mode I became smaller in diameter, and both Modes I and II decreased in number concentration. By HAB=47 mm Mode I is no longer observable.

(a)   (b)
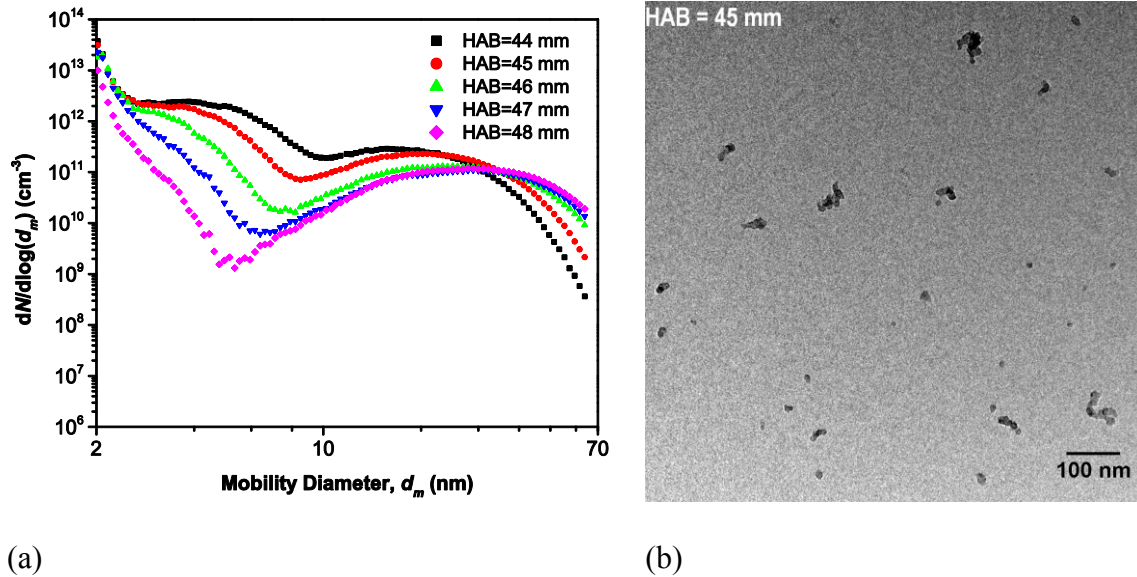
Figure 3.10. (a) Particle size distributions for HAB=44–48 mm in pure methane flame. (b) TEM image from HAB=45 mm.

The TEM image from HAB=45 mm demonstrates that at this height the soot structure is a blend of large aggregates and individual primary soot particles which proves that particles in this region of the flame are experiencing coagulation and growing in size.

Figure 3.11 shows the particle size distribution from HAB=49 mm to HAB=53 mm and a TEM image from HAB=53 mm. At the heights of 50 mm to 52 mm, the PSDs were approximately unimodal and the median particles continued to grow to ~33 nm and their number concentration decreased, likely due to coagulation. It should be noted that the inception mode remained more or less unchanged up to HAB=48 mm; however, at higher HABs the concentration of the inception tail reduced.
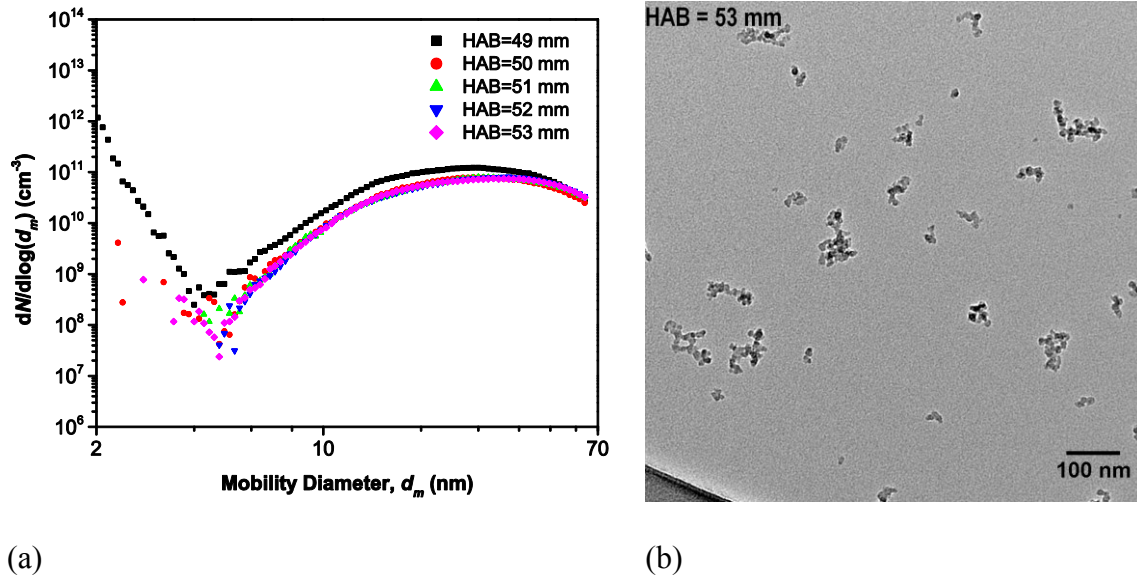
Figure 3.11. (a) Particle size distributions for HAB=49–53 mm in pure methane flame. (b) TEM image from HAB=53 mm.

The TEM image shows at HAB=53 mm that a majority of the particles possess an aggregate structure which is a clear indication that the most prominent process that particles are experiencing in this height range is coagulation.

Figure 3.12 shows the particle size distribution from HAB=54 mm to HAB=60 mm and a TEM image from HAB=60 mm. Particle size distribution results show that from HAB= 54 mm to the tip of the flame (~ 60 mm), the median particle diameter sharply decreased from ~32 nm to ~7 nm while its number concentration dropped significantly, presumably due to particle oxidation. The TEM images shows a considerable change in structure of particles from HAB=53 mm; the particles no longer have an aggregate structure, but now appear to be small, individual particles.
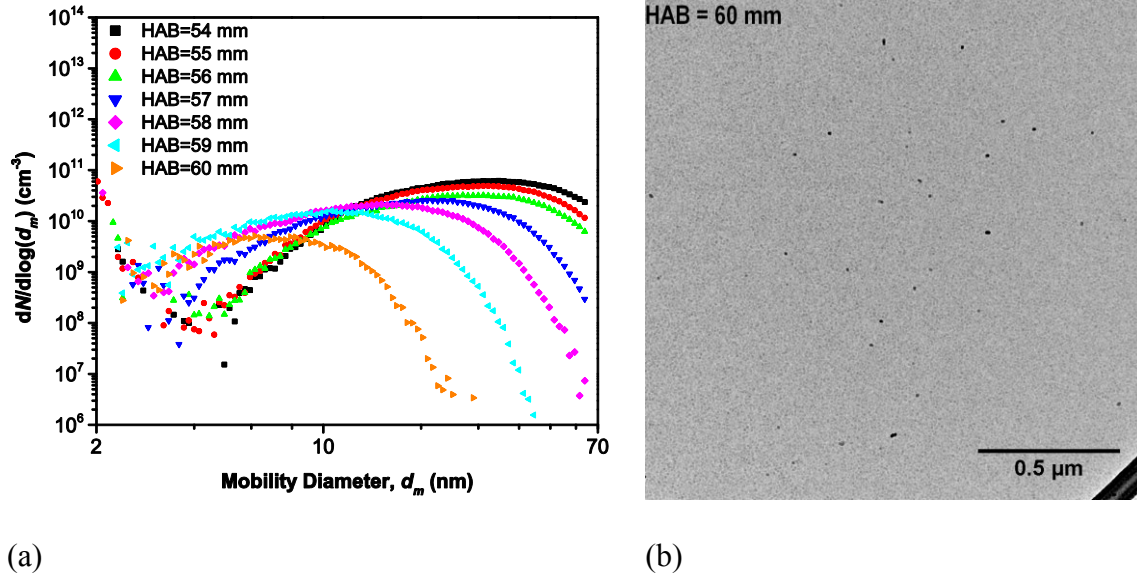
Figure 3.12. (a) Particle size distributions for HAB=54–60 mm in pure methane flame. (b) TEM image from HAB=40 mm.

The evolution of PSD was measured in diffusion flames in a number of studies (Burtscher et al. 1993; Hepp & Siegmann 1998; Kasper et al. 1999). The general trend in particle inception, coagulation and oxidation was observed by these groups; however, their results could not be compared to our results as the flames that were used in their experiments were diluted with argon which reduces the overall temperature of the flame and affects the PSDs.

On the other hand, the trend of soot particle size distribution observed in our study is similar to the evolution of soot PSD in other studies (Abid et al. 2008; Camacho et al. 2013; 2015), which were conducted on laminar premixed flames. The PSD results of the aforementioned studies also observed modes similar to Modes I and II in this study. In these studies, Mode I was affiliated with soot particle nucleation. The emergence of Mode II was claimed to be related to competitions between nucleation ,surface growth and coagulation of soot particles (Zhao et al. 2003a) .

In our study on the laminar diffusion flame, the inception mode was persistently present in the PSDs up to HAB=49 mm which confirms that soot nucleation was a major process at these heights. Results from the current diffusion flame show that the inception mode becomes very small at HABs above 53 mm. Abid et al (2009), using an nano-DMA and aerosol electrometer, measured inception mode particle throughout a premixed ethylene flame and into the post-combustion region. Zhao et al. (2005) using a similar premixed ethylene flame did not observe an inception mode throughout high temperature flames (maximum temperatures above ~1850 K). They argue that the thermal decomposition of PAH molecules at high temperatures which prevents the formation of incipient soot particles. It should be noted that the burner and fuel used by Zhao et al. (2005) and Abid et al. (2009) was not similar to the burner and fuel used in our experiments and further investigation is needed to make sure that the same PAH concentration reduction occurs in our flame.

3.3.3 Evolution of Particle Size Distribution in Methane Flame with NaCl Additive

The evolution of particle formation and growth was also investigated when NaCl particles were injected into the fuel flow. The salt particle size distribution at the fuel tube outlet was measured by connecting the fuel tube directly to the SMPS with a conductive tube (*i.e.* there was no flame and no dilution; for safety reasons the gas flow was nitrogen and not methane). Additionally, to have a better understanding of the structure of salt particles that are injected into the flame a TEM sample was taken from HAB=1 mm. Figure 3.13 shows the particle size distribution at the fuel tube outlet and TEM image of particles at HAB=1 mm. The median size of the NaCl particles was ~130 nm. The TEM image shows the NaCl particle injected possess a cubic structure.
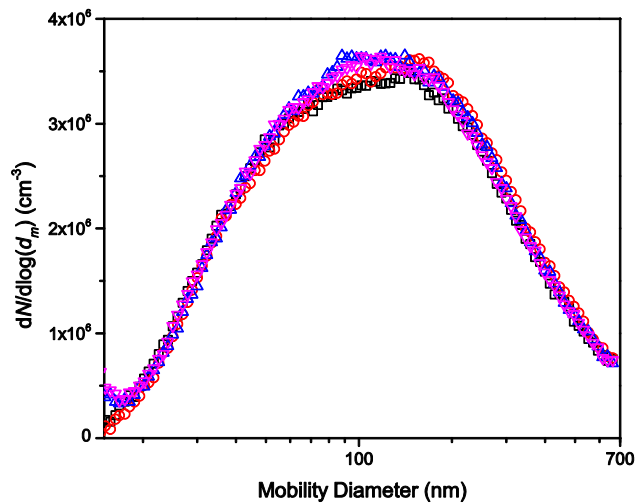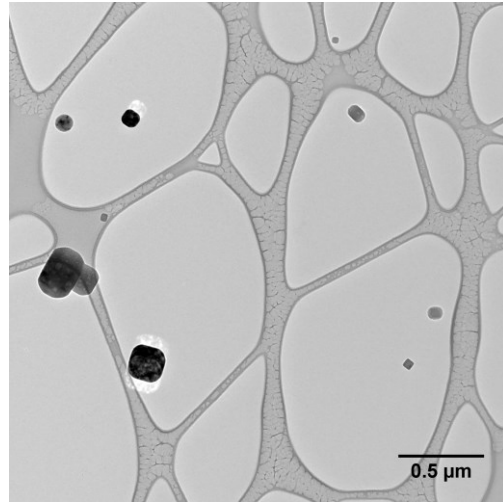
(a)   (b)

Figure 3.13. (a) The size distribution of NaCl particles at the fuel tube outlet (no flame, nitrogen as carrier gas). (b) TEM image of particles at HAB=1 mm (with flame and sampled through the usual dilution system).

Similar to the pure methane flame condition, particle size distributions at different heights above the burner were measured in the case of the methane flame doped with NaCl particles. The PSDs for HAB=8mm to HAB=26 mm and a TEM image of particles at HAB=14 mm are displayed in Figure 3.14. (Note the approximate four orders of magnitude difference in the data maximums between Figures 3.13 and 3.14.) Adding NaCl to the fuel results in the emergence of considerable amount of particles above HAB=8 mm. Recall there were no particles detected in the pure methane flame below HAB=30 mm. For these particles the PSD appears to be unimodal with a positive skew. By increasing HAB the size and number concentration of these particles reached a maximum at HAB=18 mm and decreased at higher HABs.
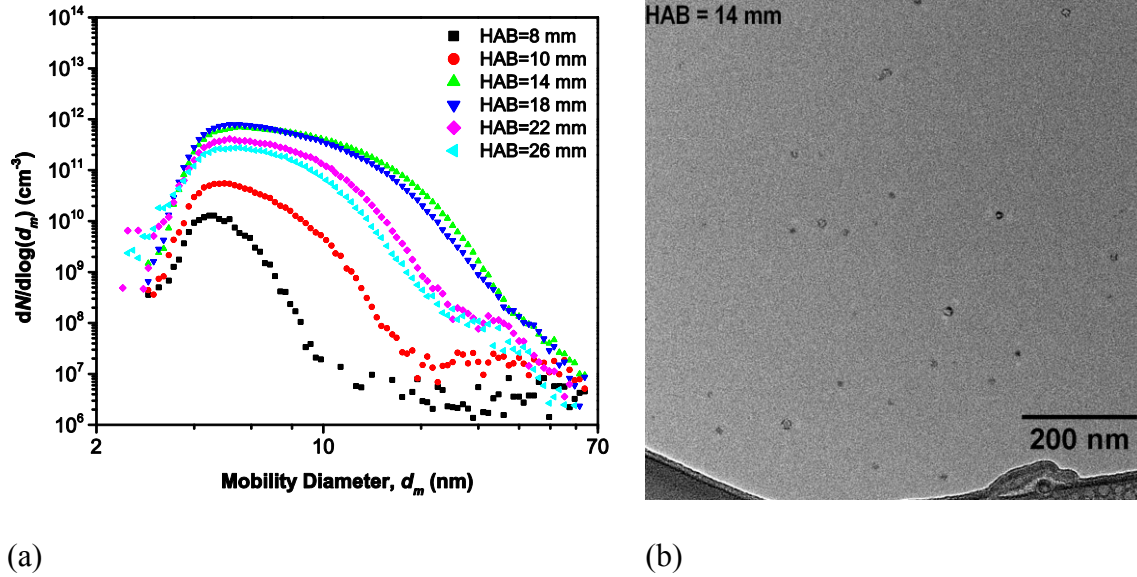
Figure 3.14. (a) Particle size distributions for HAB=8–26 mm in methane flame with NaCl additives. (b) TEM image from HAB=14 mm.

The TEM image from HAB=14 mm indicates that these particles have a non-aggregate structure and their size is relatively small. Figure 3.15 is an HRTEM image of a particle located at HAB=14 mm. The HRTEM image confirms that these particles have cubic structures which are normally associated with NaCl particles (Wang et al. 2010). Compared to the NaCl particles that were injected into the flame, NaCl particles observed from HABs above 8 mm were considerably smaller in size (median diameters of ~4–8 nm compared to 130 nm) and larger in number concentration (approximately 600 to 77000 times larger). Therefore, these NaCl particles are believed to have been formed by nucleation of condensed NaCl vapour. The contour of temperature shown in Figure 3.2 indicates that temperature of the flame at HABs below ~ 40 mm is less than the boiling temperature of NaCl; therefore, it is possible for boiled NaCl to condense at HAB below 26 mm. The NaCl vapour responsible for this particle formation may have diffused from the left or right sides of the flame where the temperature is above the boiling point of NaCl (see Figure 3.2).
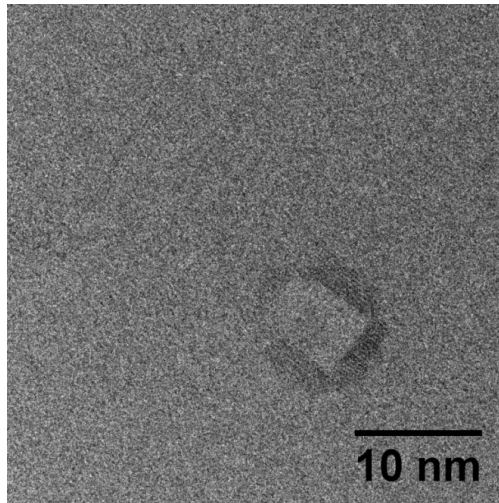
Figure 3.15. Cubic structure of a particle located at HAB=14 mm.

Figure 3.16 shows the PSDs from HAB=30 mm to HAB=38 mm. The inception mode in PSDs appears at HAB=30 mm similar to the PSDs of the pure methane flame. At HAB=30 to HAB=34 another mode was detected in the PSDs for mobility diameters greater than 5 nm which could be attributed to the remnants of NaCl particles that were formed in lower HABs. As the HAB increases the NaCl mode in the PSDs decreases in number density and was not observed above HAB=36 mm. At HAB=38 mm and above the PSDs have similar behaviour to the PSDs in the case of pure methane flame and Mode I of soot particles emerges at HAB=38 mm.
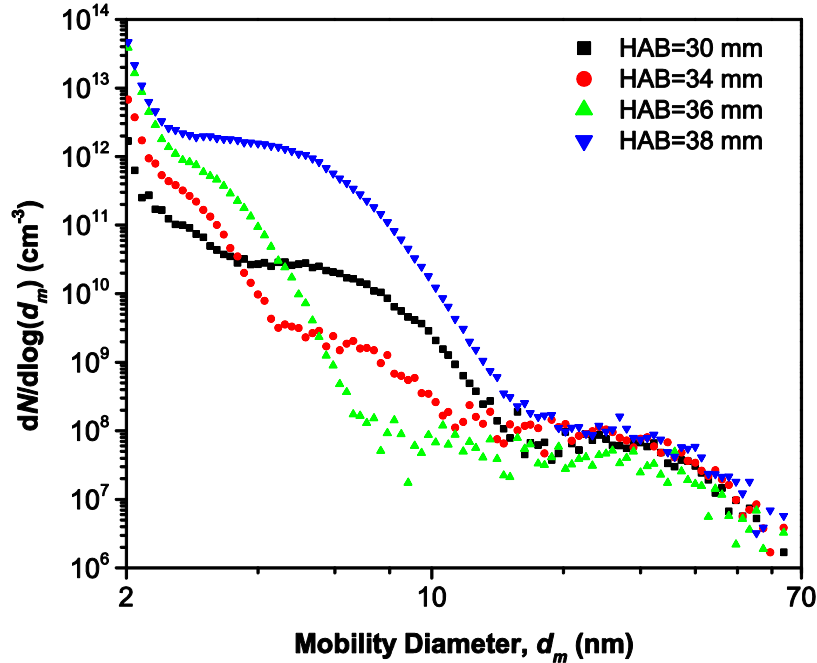
Figure 3.16. Particle size distributions for HAB=30–38 mm in methane flame with NaCl additives.

Figure 3.17 to 3.20 show the evolution of PSDs from HAB=39 mm to HAB=60 mm and TEM images from HABs=40 mm, 45 mm, 53 mm and 60 mm. The PSDs from HAB=38 mm to HAB=60 mm are quite similar to the PSDs for the pure methane flame condition with Mode I appearing at HAB=38 mm and Mode II emerging at HAB=42 mm. For HAB=47 mm to HAB=55 mm PSDs were mostly dominated by coagulation from Mode II. For HAB=56 mm to HAB=60 mm oxidation took place and a reduction in both the number concentration and particle size was observed. Although, the appearance and disappearance of the three modes is similar between the pure methane and NaCl doped flame, the median diameters and number concentrations are different, which is discussed in the next section.
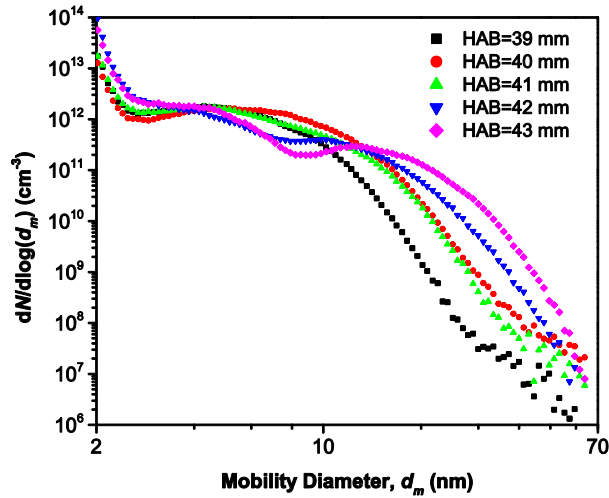
(a)
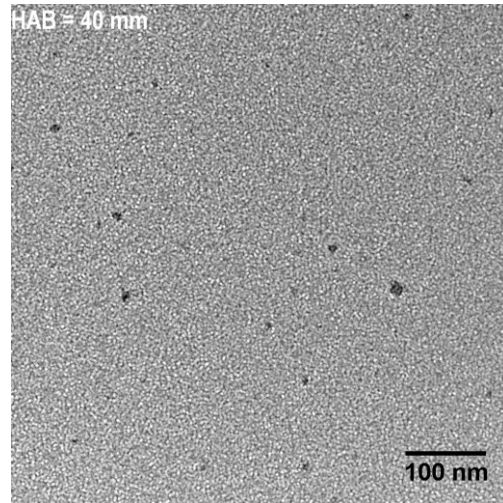
(b)

Figure 3.17. (a) Particle size distributions for HAB=39–43 mm in methane flame with NaCl additives. (b) TEM image from HAB=40 mm.
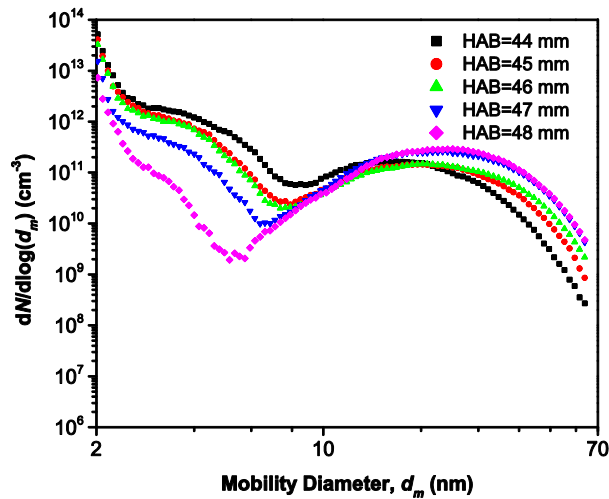
(a)
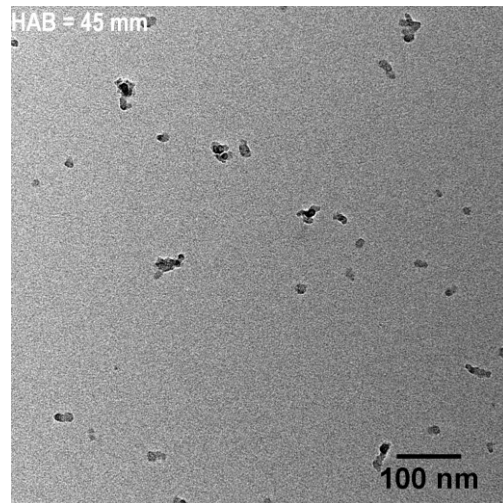
(b)

Figure 3.18. (a) Particle size distributions for HAB=44–48 mm in methane flame with NaCl additives. (b) TEM image from HAB=45 mm.
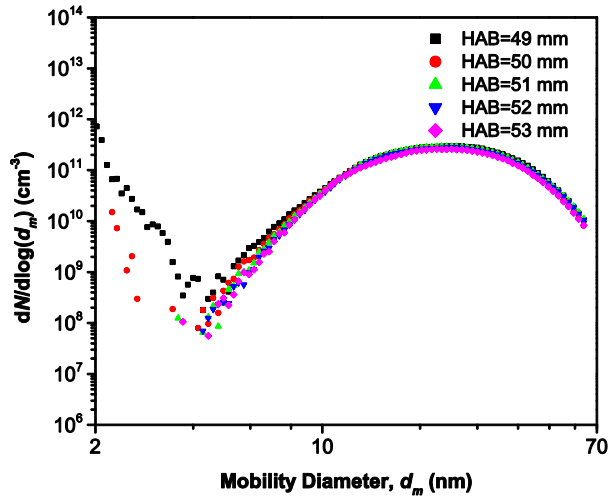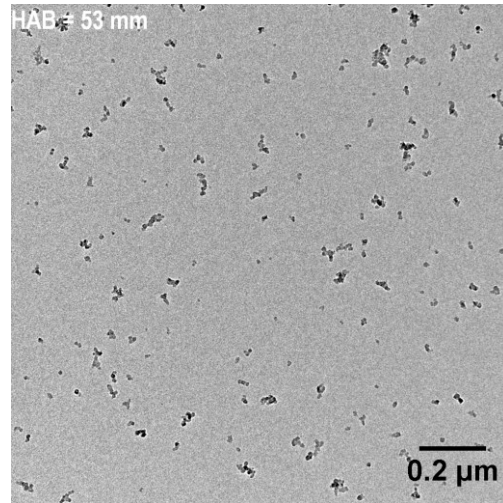
Figure 3.19. (a) Particle size distributions for HAB=49–53 mm in methane flame with NaCl additives. (b) TEM image from HAB=53 mm.
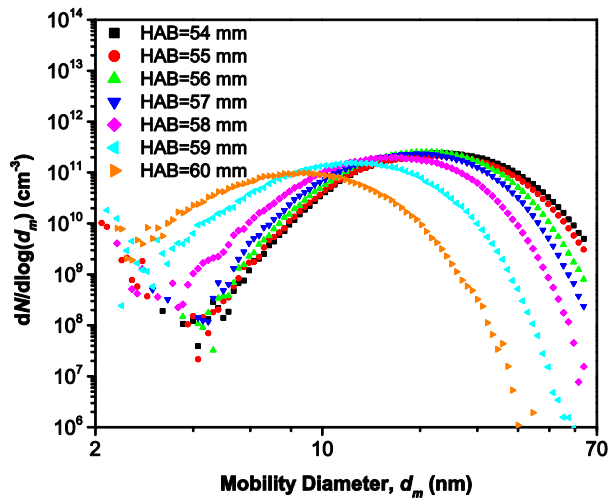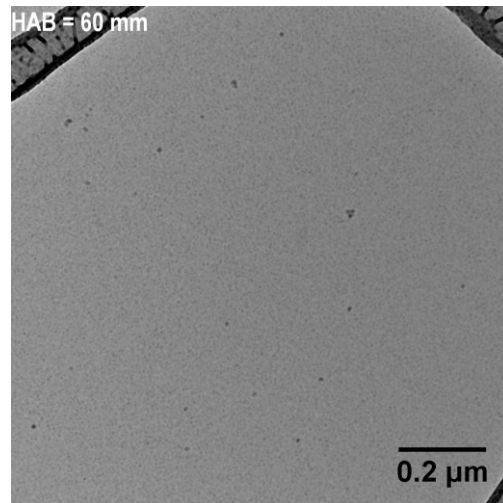
Figure 3.20. (a) Particle size distributions for HAB=54–60 mm in methane flame with NaCl additives. (b) TEM image from HAB=60 mm.

3.3.4   Comparison of Particle Size Distribution of Pure Methane Flame and Methane Flame with NaCl Additive

There are two major differences between the evolution of particles in the pure methane flame and methane flame doped with NaCl particles. The first major difference is the emergence of nano-particles with considerable concentrations at HAB=8 mm. The TEM results from HAB=14 mm confirms that these particles are NaCl particles. Traces of these particles could be found up to HAB=36 mm; however, at higher heights no sign of these particles could be found. Neither the PSDs nor the TEM images could prove that these particles still exists in a solid phase at HABs higher than 40 mm. As for HABs above 40 mm the temperature of the flame is above the boiling point it is expected that the NaCl particles have evaporated at HABs above 40 mm.

The second difference occurs at HABs above 46 mm. As mentioned earlier, at HAB=46 mm the soot particles are expected to be experiencing three simultaneous process of inception, surface growth and coagulation. For heights above 46 mm up to 53 mm, coagulation was the dominant process of soot formation which means that the sizes of particles are growing while the particle number concentration is decreasing. It appears that the rate at which the particles grow in size by increasing the HAB is quite different in each flame condition. Figure 3.20 and 3.21 illustrate the changes in median diameter and total concentration versus HABs. In the flame with NaCl additive it seems that the count median diameters of the particle distributions from HAB=47 mm to HAB=53 mm are approximately constant with a size of ~ 23 nm. For the pure methane flame the median diameter of the particles increases until it reaches a maximum of ~ 35 nm at HAB=52 mm. The results show that there is a noticeable difference between the count median diameters of the PSDs from the pure methane flame and methane flame doped with NaCl; however, in the oxidation region (HABs above 53 mm) the median diameters start to converge at regions near the tip of the flame (HAB = 60 mm). The total number concentration is quite similar for HABs

below 46 mm; however, it starts to diverge at HAB=47 mm with higher concentration of particles for flame with NaCl additives. Thus, the addition of NaCl leads to smaller particles with greater number concentrations in regions where coagulation is dominant.
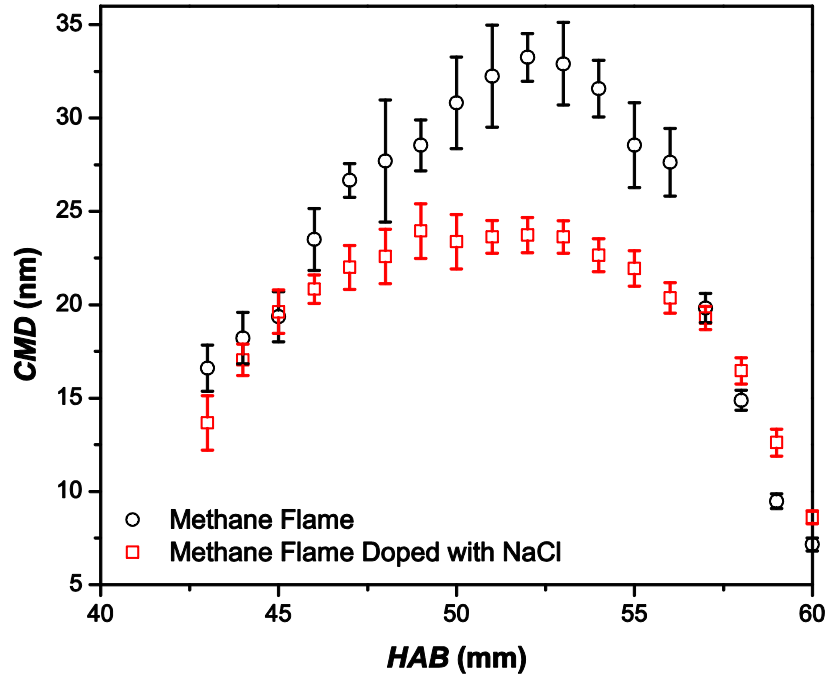
Figure 3.21. Variation of count median diameter (*CMD*) of soot particles as a function of HAB, from HAB=43 mm to HAB=60 mm for pure methane flame and methane flame with NaCl additives. The CMD was calculated for the particle size range of 2.5 nm to 64 nm.
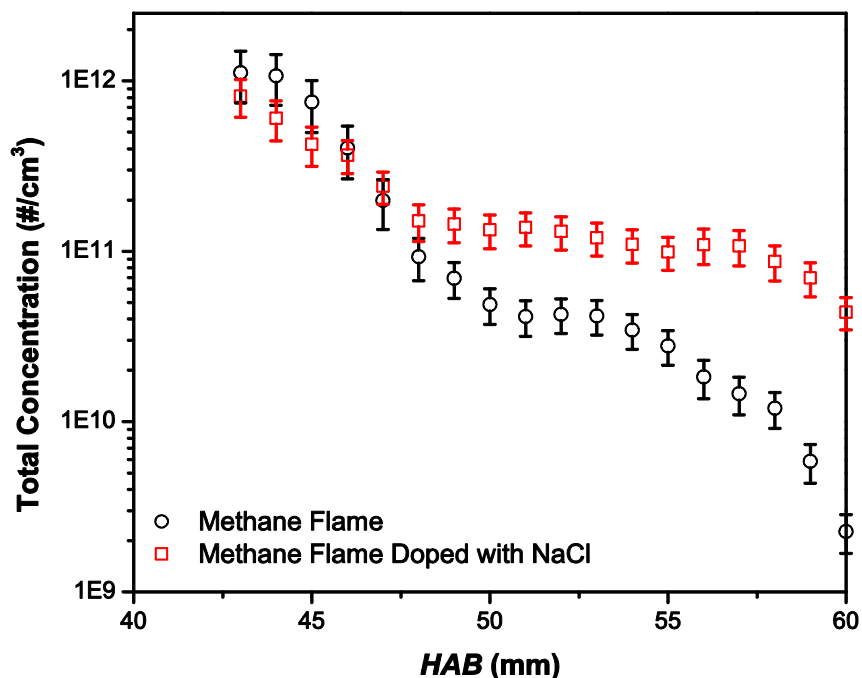
Figure 3.22. Variation of total concentration of soot particles as a function of HAB, from HAB=30 mm to HAB=60 mm for pure methane flame and methane flame with NaCl additives. The total number concentration for each set of data was measured from 2.5 nm to 64 nm.

There are two major hypotheses regarding the role of alkali metals on soot formation. Some studies suggest that alkali metals have the ability to affect the nucleation of soot particles by electrically neutralizing soot precursors and reduce soot formation (Bulewicz et al. 1975). On the other hand, a number of researchers (Howard et al. 1973; Wersborg et al. 1975; Mitchell & Miller 1989) suggested that a majority of soot particles possess positive charges, presumably due to thermionic emission. It was observed by Mitchell and Miller (1989) that the addition of alkali metals reduces the number concentration of soot particles that are positively charged and suggested that alkali metals have the ability to neutralize charges of soot particles through the following reaction:

$$M + soot^+ \rightleftarrows M^+ + soot \tag{3.1}$$

Neutral soot particles have lower tendencies to coagulate compared to populations that include both charged and neutral soot particles (Glarborg 2007). Howard et al. (1973) investigated the coagulation of soot particles in a flat premixed acetylene flame by accounting for both van der Waals and electrostatic forces and found that the coagulation rate constant between charged and uncharged particles could increase up to 2 or 3 times due to the aforementioned forces. It has also been mentioned (Haynes et al. 1979) that the addition of sodium, potassium and cesium to a premixed ethylene-air flame led to reduction in the size of soot particles.

The results acquired from our experiments confirm that NaCl addition reduced the agglomeration of particles, as the median size of particles in the regions of the flame where aggregation was taking place were smaller compared to the pure methane flame and the number densities of particles were higher which is in agreement with the second hypothesis. Therefore, the reduction of particle coagulation could be attributed to the effect of alkali metal (in this case sodium from NaCl) on soot particles.

Chapter 4

Conclusions and Recommendations

Flares used in the upstream oil and gas industries could be contaminated with produced water compounds from oil and gas wells and these compounds, which mostly consist of Na and Cl, could affect the formation of particles in flares. Flares used in the upstream oil and gas industries are diffusion flames. In this study the evolution of particles and their morphology along the centerline of a laminar diffusion flame and the effect of NaCl addition on particle formation was investigated.

This investigation was performed on a 10 mm diameter Santora (laminar co-flow) burner that produced a conical flame approximately 60 mm in height. A sampling system was designed to extract aerosol samples from different heights above the burner (HAB) and transfer them to scanning mobility particle sizer (SMPS) for measuring the soot particle size distribution (PSD). The most important feature of the sampling system was its ability to provide a wide range of dilution for the extracted samples, which minimized coagulation of extracted aerosol samples. A temperature measurement system was designed based on Cundy (1986) to measure the gas temperature from different regions of the flame, with a rapid thermocouple insertion technique.

The radial temperature profile of the flame was measured for both cases of the pure methane flame and the methane flame doped with NaCl. In addition the effect of the probe on the temperature profile along the centerline of the flame was investigated and it was found that the probe starts to affect the temperature of the flame from locations approximately 3 mm below the

probe. At the vicinity of the probe the temperature could drop as much as 600 K at the hottest parts of the flame.

The effect of dilution on particle size distribution was studied by changing the dilution ratio of the extracted sample. It was found that dilution ratio could significantly affect the size distribution of particles and inadequate dilution could lead to coagulation of aerosol samples and result in particles with greater sizes and lower number concentration, which are no representative of the actual particles in the flame.

The evolution of nano-particles on the centerline of the pure methane flame was inspected by measuring the PSDs of soot particles at different HABs. The results show that nano-particles; with sizes mostly below 3 nm, start to emerge from HAB=30 mm and these particles are assumed to be the incipient soot particles. As HAB increases the PSDs grow in size and number and at HAB=38 mm a mode starts to form for particles above 5 nm in addition to the sub 3 nm particles. By further increasing the height at HAB=43 mm the mode splits into a bimodal distribution of particles with the smaller mode being between 3 to 10 nm and the larger mode being greater than 10 nm. The smaller mode is referred to as Mode I, and the larger mode is referred to as Mode II. For HABs greater than 43 mm the number concentration and size of particles of Mode I reduced and at HAB=48 mm it disappeared. Though not measured directly, the sub-3 nm particles start to disappear at HABs above 50 mm. On the other hand, for HABs above 43 nm the size of particles in Mode II grows and the number concentration decreases which is an indication that coagulation is the predominant process for particles in Mode II and this trend continues until HAB=52 mm. For HABs greater than 52 mm the size and number concentration of particles decrease which indicates that the particles are oxidizing and at HABs near the tip of the flame the concentration and size of particles drop significantly.

From TEM images it was concluded that at the early stages of soot formation and growth, soot particles possess a non-aggregate structures. As the HAB increases, a portion of particles transforms into aggregates and in the HABs where coagulation is dominant the particles are mostly aggregates. Finally at regions near the tip of the flame where oxidation is the governing mechanism particles transform from aggregate to individual non-aggregate structures with considerably smaller sizes. The use of HRTEM, demonstrated the structure of single individual soot particles at the early stages of soot formation. Based on the HRTEM images individual soot particles consisted of core shell structures and some particles possessed multiple cores with multiple concentric shells.

The evolution of soot particle size distribution was also measured for the methane flame doped with NaCl particles. NaCl particles were injected to the fuel and the same process for evaluating the evolution of nano-particles was repeated for the case of the flame doped with NaCl particles. Results show the emergence of a significant number of particles with unimodal distributions at relatively low HABs (8 mm) of the flame where the formation of nano-particles was not observed in the case of the pure methane flame. By increasing the HAB the number concentration of these particles increased until it reached a maximum at HAB=18 mm, followed by a decrease in size and number of particles. TEM and HRTEM confirms that the structure of the particles is cubic and are presumably evaporated NaCl particles that have diffused to cooler region of flow, condensed and nucleated to form these particles. The PSD results also show that soot particles start to emerge at HAB=30 mm and the trend of soot evolution were approximately similar to the pure methane flame, except in magnitude.

Comparing the evolution of PSDs from both cases revealed that there are two major differences between nano-particle evolution in the pure methane flame and methane flame doped with NaCl

70

particles. The first difference is the emergence of a considerable concentration of NaCl particles at low HABs. The temperature profile of the flame doped with NaCl suggests that these NaCl particles are presumably formed due to condensation of evaporated NaCl particles that have been diffused to cooler regions of the flow.

The second difference is related to the PSD evolution where soot particles are the dominant nano-particles. Unlike the qualitative similarities in PSD evolution for HABs above 30 mm in both cases of the pure methane flame and methane flame doped with NaCl particles, there exists quantitative differences. These differences were mostly from regions of the flame where coagulation is the dominating process in soot formation (HAB=43 mm – 52 mm). In this region of the flame the count median diameter of PSDs of the methane flame doped with NaCl particles is smaller compared to the count median diameter of particles in the pure methane flame. On the other hand, the number concentration of particles for the methane flame with NaCl additives is larger compared to the pure methane flame. It is speculated that NaCl particles could reduce the coagulation process between soot particles which results in smaller particles with larger number concentrations. Based on previous studies (Mitchell and Miller 1989; Glarborg 2007) this trend could be attributed to the sodium content of NaCl that can remove electrical charges from soot particles and make them neutral which subsequently reduces the coagulation between soot particles.

4.1 Recommendations and Future Works

4.1.1 Experimental Set-up Improvements

One of the most critical parameters in this study is the dilution ratio. Measurement of the dilution ratio is highly dependent on the readings from gas analyzers. The gas analyzer used for measurements in the diluted condition needed to read very low concentrations of CO_2 for reaching high dilution ratio. Using a GC gas analyzer instead of an NDIR could increase the precision of measurements in low ppm CO_2 concentrations and reduce the uncertainties of dilution ratio.

Additionally the undiluted sampling system could be further improved to have more accurate measurements of CO_2. In our study the concentration of CO_2 was estimated based on dry CO_2 concentration as the gas analyzer used for low dilutions could not measure the concentration of CO_2 in high humidity. It is possible to use other gas analyzers that can measure the concentration of CO_2 in high humidifies or measure the concentration of H_2O with a dew point meter as was done in (Mitchell 1975) and correct the concentration of dry CO_2 using the current experimental set-up.

4.1.2 2D Mapping of Size Distributions

Results from this study provided insightful information on the evolution of soot PSD along centerline of the flame. The temperature gradient in the radial position of the flame is more steep than along the centerline of the flame. This temperature gradient could affect the evolution of soot particles along the radial positions as the process of soot formation highly dependent on temperature. A more thorough picture of soot evolution could be achieved if the evolution of the soot PSDs at radial location could be measured as well.

4.1.3   Change of Flame Temperature

As mentioned in Section 1.5.2, PAHs reactions with different intermediate species leads to soot nucleation and those reactions are highly temperature dependent. It is possible to reduce the temperature of the flame by doping the fuel with inert gases such as argon and investigate the changes in soot morphology and PSD evolution at lower temperatures.

4.1.4   The Use of Other Fuels

Methane was a simplistic representative of the associated gas burnt in flares. On the one hand, in future studies the composition of the flame fuel could be altered to make it more similar to the composition of associated gas by adding other hydrocarbons such as ethane and propane. On the other hand, ethylene was used as the fuel in numerous studies conducted on PSD evolution of soot in premixed flames (Zhao et al. 2003b; Abid et al. 2008). The same methods in the current study could be applied on an ethylene diffusion flame and the results could be compared with the studies conducted by other groups on premixed ethylene flames.

4.2   Other Alkali Additive

The composition of the flowback water (Table 1.1) shows other cations such as calcium, potassium and magnesium. Studies have shown that potassium could greatly affect the formation of soot particles (Mitchell & Miller 1989; Tappe et al. 1993). Although the concentration of alkali chlorides such as KCl is considerably lower than NaCl in the representative solution, it is worthwhile to investigate the addition of miniscule concentrations of potassium as the experimental results from other studies indicates that this cation can affect the formation of soot particles in flames more than sodium.

Bibliography

Abid, A.D. (2009). *Experimental investigation of soot nucleation and growth in premixed flat flames*. PhD degree dissertation, University of Southern California, Los Angeles, CA.

Abid, A.D., Heinz, N., Tolmachoff, E.D., Phares, D.J., Campbell, C.S. & Wang, H. (2008). On evolution of particle size distribution functions of incipient soot in premixed ethylene-oxygen-argon flames. *Combustion and Flame*, 154(4):775–788.

Abid, A.D., Tolmachoff, E.D., Phares, D.J., Wang, H., Liu, Y. & Laskin, A. (2009). Size distribution and morphology of nascent soot in premixed ethylene flames with and without benzene doping. *Proceedings of the Combustion Institute*, 32(1):681–688.

Acharya, H.R., Henderson, C., Matis, H., Kommepalli, H., Moore, B. & Wang, H. (2011). Cost Effective Recovery of Low-TDS Frac Flowback Water for Re-use. *DOE Report DE-FE0000784*:1–100.

Alberta Energy Regulator (2016). *Upstream Petroleum Industry Flaring, Incinerating, and Venting: Industry Performance for Year Ending December 31, 2014*, Calgary, AB, Canada.

An, Y.Z., Li, X., Teng, S.P., Wang, K., Pei, Y.Q., Qin, J. & Zhao, H. (2016). Development of a soot particle model with PAHs as precursors through simulations and experiments. *Fuel*, 179:246–257.

Ballantyne, A. & Moss, J.B. (1977). Fine Wire Thermocouple Measurements of Fluctuating Temperature. *Combustion Science and Technology*, 17(1–2):63–72.

Barbot, E., Vidic, N.S., Gregory, K.B. & Vidic, R.D. (2013). Spatial and temporal correlation of water quality parameters of produced waters from Devonian-age shale following hydraulic fracturing. *Environmental Science and Technology*, 47(6):2562–2569.

Blondes, M.S., Gans, K.D., Thordsen, J.J., Reidy, M.E., Thomas, B., Engle, M.A., Kharaka, Y.K. & Rowan, E.L. (2014). U.S. Geological Survey National Produced Waters Geochemical Database v2.1 (PROVISIONAL). *United States Geological Survey*.

Bonczyk, P.A. (1988). Suppression of Soot in Flames by Alkaline-Earth and Other Metal Additives. *Combustion Science and Technology*, 59(1–3):143–163.

Bond, T.C. & Sun, H. (2005). Can reducing black carbon emissions counteract global warming? *Environmental Science and Technology*, 39(16):5921–5926.

Botero, M.L., Chen, D., González-Calera, S., Jefferson, D. & Kraft, M. (2016). HRTEM evaluation of soot particles produced by the non-premixed combustion of liquid fuels. *Carbon*, 96:459–473.

Bradley, D. & Entwistle, a G. (1961). Determination of the emissivity, for total radiation, of small diameter platinum-10% rhodium wires in the temperature range 600-1450 C. *British Journal of Applied Physics*, 12:708–711.

Bulewicz, E.M., Evans, D.G. & Padley, P.J. (1975). Effect of metallic additives on soot formation processes in flames. *Symposium (International) on Combustion*, 15(1):1461–1470.

Burtscher, H., Matter, D. & Siegmann, H.C. (1993). Measurement of size distribution and photoelectric activity of particles in a gas diffusion flame. *Atmospheric Environment Part A, General Topics*, 27(8):1255–1259.

Camacho, J., Lieb, S. & Wang, H. (2013). Evolution of size distribution of nascent soot in n- and i-butanol flames. *Proceedings of the Combustion Institute*, 34(1):1853–1860.

Camacho, J., Liu, C., Gu, C., Lin, H., Huang, Z., Tang, Q., You, X., Saggese, C., Li, Y., Jung, H., Deng, L., Wlokas, I. & Wang, H. (2015). Mobility size and mass of nascent soot particles in a benchmark premixed ethylene flame. *Combustion and Flame*, 162(10):3810–3822.

Chapman, E.C., Capo, R.C., Stewart, B.W., Kirby, C.S., Hammack, R.W., Schroeder, K.T. & Edenborn, H.M. (2012). Geochemical and strontium isotope characterization of produced waters from marcellus shale natural gas extraction. *Environmental Science and Technology*, 46(6):3545–3553.

Chen, H.X. & Dobbins, R.A. (2000). Crystallogenesis of Particles Formed in Hydrocarbon Combustion. *Combustion Science and Technology*, 159(1):109–128.

Crosland, B.M., Johnson, M.R. & Thomson, K.A. (2011). Analysis of uncertainties in instantaneous soot volume fraction measurements using two-dimensional, auto-compensating, laser-induced incandescence (2D-AC-LII). *Applied Physics B: Lasers and Optics*, 102(1):173–183.

Cundy, V.A., Morse, J.S. & Senser, D.W. (1986). Constant-tension thermocouple rake suitable for use in flame mode combustion studies. *Review of Scientific Instruments*, 57(6):1209–1210.

Dasch, C.J. (1985). New soot diagnostics in flames based on laser vaporization of soot. *Symposium (International) on Combustion*, 20(1):1231–1237.

Dobbins, R.A., Fletcher, R.A. & Chang, H.C. (1998). The evolution of soot precursor particles in a diffusion flame. *Combustion and Flame*, 115(3):285–298.

Elvidge, C.D., Zhizhin, M., Baugh, K., Hsu, F.C. & Ghosh, T. (2016). Methods for global survey of natural gas flaring from visible infrared imaging radiometer suite data. *Energies*, 9(1):14.

Fawole, O.G., Cai, X.M. & Mackenzie, A.R. (2016). Gas flaring and resultant air pollution: A review focusing on black carbon. *Environmental Pollution*, 216:182–197.

De Filippo, A., Sgro, L.A., Lanzuolo, G. & D'Alessio, A. (2009). Probe measurements and numerical model predictions of evolving size distributions in premixed flames. *Combustion and Flame*, 156(9):1744–1754.

Frenklach, M. (2002). Reaction mechanism of soot formation in flames. *Physical Chemistry*

Chemical Physics, 4(11):2028–2037.

Frenklach, M. & Wang, H. (1991). Detailed modeling of soot particle nucleation and growth. *Symposium (International) on Combustion*, 23(1):1559–1566.

Giechaskiel, B., Maricq, M., Ntziachristos, L., Dardiotis, C., Wang, X., Axmann, H., Bergmann, A. & Schindler, W. (2014). Review of motor vehicle particulate emissions sampling and measurement: From smoke and filter mass to particle number. *Journal of Aerosol Science*, 67:48–86.

Glarborg, P. (2007). Hidden interactions-Trace species governing combustion and emissions. *Proceedings of the Combustion Institute*, 31(1):77–98.

Gregory, K.B., Vidic, R.D. & Dzombak, D.A. (2011). Water management challenges associated with the production of shale gas by hydraulic fracturing. *Elements*, 7(3):181–186.

Gröhn, A.J., Eggersdorfer, M.L., Pratsinis, S.E. & Wegner, K. (2014). On-line monitoring of primary and agglomerate particle dynamics. *Journal of Aerosol Science*, 73:1–13.

Haluszczak, L.O., Rose, A.W. & Kump, L.R. (2013). Geochemical evaluation of flowback brine from Marcellus gas wells in Pennsylvania, USA. *Applied Geochemistry*, 28:55–61.

Hayes, T. & Severin, B.F. (2012). Barnett and Appalachian Shale Water Management and Reuse Technologies. *Rep. no. 8122-05, Research Partnership to Secure Energy for America*.

Haynes, B.S., Jander, H. & Wagner, H.G.G. (1979). The effect of metal additives on the formation of soot in premixed flames. *Symposium (International) on Combustion*, 17(1):1365–1374.

Haynes, B.S. & Wagner, H.G. (1981). Soot Formation. *Progress in Energy and Combustion Science*, 7(4):229–273.

Heitor, M. V. & Moreira, A.L.N. (1993). Thermocouples and sample probes for combustion studies. *Progress in Energy and Combustion Science*, 19(3):259–278.

Hepp, H. & Siegmann, K. (1998). Mapping of soot particles in a weakly sooting diffusion flame by aerosol techniques. *Combustion and Flame*, 115(1–2):275–283.

Higgins, K.J., Jung, H., Kittelson, D.B., Roberts, J.T. & Zachariah, M.R. (2002). Size-selected nanoparticle chemistry: Kinetics of soot oxidation. *Journal of Physical Chemistry A*, 106(1):96–103.

Hinds, W.C. (1999). *Aerosol technology: properties, behaviour, and measurement of airborne particles* Second Edi., John Wiley & Sons.

Horner, P., Halldorson, B. & Slutz, J. (2011). Shale Gas Water Treatment Value Chain-A Review of Technologies including Case Studies. In *SPE Annual Technical Conference*. Society of Petroleum Engineers.

Howard, J.B. (1991). Carbon addition and oxidation reactions in heterogeneous combustion and soot formation. *Symposium (International) on Combustion*, 23(1):1107–1127.

Howard, J.B., Wersborg, B.L. & Williams, G.C. (1973). Coagulation of carbon particles in premixed flames. *Faraday Symposia of the Chemical Society*, 7(2):109–119.

Johnson, M.R. & Coderre, A.R. (2011). An Analysis of Flaring and Venting Activity in the Alberta Upstream Oil and Gas Industry. *Journal of the Air & Waste Management Association*, 61(2):190–200.

Johnson, M.R., Kostiuk, L.W. & Spangelo, J.L. (2001a). A characterization of solution gas flaring in Alberta. *Journal of the Air & Waste Management Association*, 51(8):1167–1177.

Johnson, M.R., Kostiuk, L.W. & Spangelo, J.L. (2001b). A characterization of solution gas flaring in Alberta. *Journal of the Air & Waste Management Association (1995)*, 51(8):1167–1177.

Kasper, M., Sattler, K., Siegmann, K., Matter, U. & Siegmann, H.C. (1999). The influence of fuel addititive on the formation of carbon during combustion. *Journal of Aerosol Science*, 30(2):217–225.

Kasper, M., Siegmann, K. & Sattler, K. (1997). Evaluation of an in situ sampling probe for its accuracy in determining particle size distributions from flames. *Journal of Aerosol Science*, 28(8):1569–1578.

Katsuki, M., Mizutani, Y. & Matsumoto, Y. (1987). An improved thermocouple technique for measurement of fluctuating temperatures in flames. *Combustion and Flame*, 67(1):27–36.

Kazemimanesh, M. (2014). *Effects of Non-hydrocarbon Liquids on Particulate Emissions of Flares*. Master's thesis. University of Alberta, Edmonton, AB.

Kazemimanesh, M., Moallemi, A., Olfert, J.S. & Kostiuk, L.W. (2016). Probe sampling to map and characterize nanoparticles along the axis of a laminar methane jet diffusion flame. *Proceedings of the Combustion Institute.*, (in press):doi: 10.1016/j.proci.2016.06.169.

Kholghy, M.R. (2012). *The Evolution of Soot Morphology in Laminar Co-Flow Diffusion Flames of the Surrogates for Jet A-1 and a Synthetic Kerosene*. masters thesis. University of Toronto, Toronto, ON.

Kholghy, M.R., Saffaripour, M., Yip, C. & Thomson, M.J. (2013). The evolution of soot morphology in a laminar coflow diffusion flame of a surrogate for Jet A-1. *Combustion and Flame*, 160(10):2119–2130.

Kholghy, M.R., Weingarten, J. & Thomson, M.J. (2015). A study of the effects of the ester moiety on soot formation and species concentrations in a laminar coflow diffusion flame of a surrogate for B100 biodiesel. *Proceedings of the Combustion Institute*, 35(1):905–912.

Koch, D. & Hansen, J. (2005). Distant origins of Arctic black carbon: A Goddard Institute for Space Studies ModelE experiment. *Journal of Geophysical Research: Atmospheres*, 110(4):1–14.

Krüger, V., Wahl, C., Hadef, R., Geigle, K.P., Stricker, W. & Aigner, M. (2005). Comparison of laser-induced incandescence method with scanning mobility particle sizer technique: the

influence of probe sampling and laser heating on soot particle size distribution. *Measurement Science and Technology*, 16(7):1477–1486.

Maricq, M. (2011). Physical and chemical comparison of soot in hydrocarbon and biodiesel fuel diffusion flames: A study of model and commercial fuels. *Combustion and Flame*, 158(1):105–116.

Maricq, M. (2012). Soot formation in ethanol/gasoline fuel blend diffusion flames. *Combustion and Flame*, 159(1):170–180.

Maricq, M.M., Harris, S.J. & Szente, J.J. (2003). Soot size distributions in rich premixed ethylene flames. *Combustion and Flame*, 132(3):328–342.

Maricq, M.M. & Xu, N. (2004). The effective density and fractal dimension of soot particles from premixed flames and motor vehicle exhaust. *Journal of Aerosol Science*, 35(10):1251–1274.

McElreath, D. (2011). Comparison of Hydraulic Fracturing Fluids Composition with Produced Formation Water following Fracturing – Implications for Fate and Transport. In *Proceedings of the Technical Workshops for the Hydraulic Fracturing Study: Fate and Transport*. Washington, DC.

McEnally, C.S., Köylü, Ü.Ö., Pfefferle, L.D. & Rosner, D.E. (1997). Soot volume fraction and temperature measurements in laminar nonpremixed flames using thermocouples. *Combustion and Flame*, 109(4):701–720.

McEwen, J.D.N. (2010). *Soot Emission Factors from Lab-Scale Flares Burning Solution Gas Mixtures*. Master's thesis, Carleton University, Ottawa, ON.

McEwen, J.D.N. & Johnson, M.R. (2012). Black carbon particulate matter emission factors for buoyancy-driven associated gas flares. *Journal of the Air & Waste Management Association*, 62(3):307–321.

Menon, S., Hansen, J., Nazarenko, L., Luo, Y., Husar, R.B., Xu, Q., Hansen, J., Sato, M., Ruedy, R., Lacis, A., Oinas, V., Jacobson, M., Novakov, T., Streets, D.G., Kaufman, Y.J., Fraser, R.S., Rosenfeld, D., Rudich, Y., Lahav, R., Rotstayn, L.D., Lohmann, U., Luo, Y., Daren, L., Zhou, X., Li, W., He, Q., Collins, W.D., Ramanathan, V., Lau, K.-M., Li, M.-T., Kim, J.H., Sud, Y., Dazlich, D.A., Corsetti, T.G., Kaiser, D.P., Bradley, R.S., Keimig, F.T., Norris, J.R., Ackerman, A.S. & Kunzli, N. (2002). Climate effects of black carbon aerosols in China and India. *Science*, 297(5590):2250–3.

Michelsen, H.A. (2016). Probing soot formation, chemical and physical evolution, and oxidation: A review of in situ diagnostic techniques and needs. *Proceedings of the Combustion Institute*, (in press):doi: 10.1016/j.proci.2016.08.027.

Miller, D.J., Huang, X., Li, H., Kasemset, S., Lee, A., Agnihotri, D., Hayes, T., Paul, D.R. & Freeman, B.D. (2013). Fouling-resistant membranes for the treatment of flowback water from hydraulic shale fracturing: A pilot study. *Journal of Membrane Science*, 437:265–275.

Mitchell, J.B.A. & Miller, D.J.M. (1989). Studies of the effects of metallic and gaseous additives

in the control of soot formation in diffusion flames. *Combustion and Flame*, 75(1):45–55.

Mitchell, R.E. (1975). *Nitrogen oxide formation in laminar methane-air diffusion flames (Doctoral dissertation)*. PhD thesis, Massachusetts Institute of Technology, Boston, MA.

Ni, T., Gupta, S.B. & Santoro, R.J. (1994). Suppression of soot formation in ethene laminar diffusion flames by chemical additives. *Symposium (International) on Combustion*, 25(1):585–592.

Oberdörster, G., Sharp, Z., Atudorei, V., Elder, A., Gelein, R., Kreyling, W. & Cox, C. (2004). Translocation of Inhaled Ultrafine Particles to the Brain. *Inhalation Toxicology*, 16(6–7):437–445.

Paktinat, J., Neil, B.O. & Tulissi, M. (2011). Case Studies : Impact of High Salt Tolerant Friction Reducers on Fresh Water Conservation in Canadian Shale Fracturing Treatments. In *Canadian Unconventional Resources and International Petroleum Conference*. Society of Petroleum Engineers.

Park, J.H., Mudunkotuwa, I.A., Mines, L.W.D., Anthony, T.R., Grassian, V.H. & Peters, T.M. (2015). A Granular Bed for Use in a Nanoparticle Respiratory Deposition Sampler. *Aerosol Science and Technology*, 49(3):179–187.

Pedata, P., Bergamasco, N., D'Anna, A., Minutolo, P., Servillo, L., Sannolo, N. & Balestrieri, M.L. (2013). Apoptotic and proinflammatory effect of combustion-generated organic nanoparticles in endothelial cells. *Toxicology Letters*, 219(3):307–314.

Ramanathan, V. & Carmichael, G. (2008). Global and regional climate changes due to black carbon. *Nature Geoscience*, 1:221–227.

Saffaripour, M., Zabeti, P., Kholghy, M. & Thomson, M.J. (2011). An experimental comparison of the sooting behavior of synthetic jet fuels. *Energy and Fuels*, 25(12):5584–5593.

Santoro, R.J., Semerjian, H.G. & Dobbins, R.A. (1983). Soot particle measurements in diffusion flames. *Combustion and Flame*, 51:203–218.

Santoro, R.J., Yeh, T.T., Horvath, J.J. & Semerjian, H.G. (1987). The Transport and Growth of Soot Particles in Laminar Diffusion Flames. *Combustion Science and Technology*, 53(2–3):89–115.

Sato, M., Hansen, J., Koch, D., Lacis, A., Ruedy, R., Dubovik, O., Holben, B., Chin, M. & Novakov, T. (2003). Global atmospheric black carbon inferred from AERONET. *Proceedings of the National Academy of Sciences of the United States of America*, 100(11):6319–24.

Schweitzer, D. (2010). Oil companies and sustainability: More than just an image? Available at: http://deepblue.lib.umich.edu/bitstream/handle/2027.42/77607/dschwei.pdf.

Sgro, L.A., Barone, A.C., Commodo, M., D'Alessio, A., De Filippo, A., Lanzuolo, G. & Minutolo, P. (2009). Measurement of nanoparticles of organic carbon in non-sooting flame conditions. *Proceedings of the Combustion Institute*, 32(1):689–696.

Shaddix, C.R. (1999). Correcting thermocouple measurements for radiation loss: a critical review. In *Proceedings of the 33rd National Heat Transfer Conference*. Albuquerque, NM.

Shaddix, C.R. & Smyth, K.C. (1996). Laser-induced incandescence measurements of soot production in steady and flickering methane, propane, and ethylene diffusion flames. *Combustion and Flame*, 107(4):418–452.

Siegmann, K., Sattler, K. & Siegmann, H.C. (2002). C lustering at high temperatures: carbon formation in combustion. *Journal of Electron Spectroscopy and Related Phenomena*, 126:191–202.

Simonsson, J., Olofsson, N.E., Bladh, H., Sanati, M. & Bengtsson, P.E. (2016). Influence of potassium and iron chloride on the early stages of soot formation studied using imaging LII/ELS and TEM techniques. *Proceedings of the Combustion Institute*, (in press):10.1016/j.proci.2016.07.003.

Slutz, J., Anderson, J., Broderick, R. & Horner, P. (2012). Key Shale Gas Water Management Strategies: An Economic Assessment Tool. In *In International Conference on Health, Safety and Environment in Oil and Gas Exploration and Production*. Society of Petroleum Engineers.

Snelling, D.R., Liu, F., Smallwood, G.J. & Gülder, Ö.L. (2004). Determination of the soot absorption function and thermal accommodation coefficient using low-fluence LII in a laminar coflow ethylene diffusion flame. *Combustion and Flame*, 136(1–2):180–190.

Solomon, S., Qin, D., Manning, M., Alley, R.B., Berntsen, T., Bindoff, N.L., Chen, Z., Chidthaisong, A., Gregory, J.M., Hegerl, G.C., Heimann, M., Hewitson, B., Hoskins, B.J., Joos, F., Jouzel, J., Kattsov, V., Lohmann, U., Matsuno, T., Molina, M., Nicholls, N., Overpeck, J., Raga, G., Ramaswamy, V., Ren, J., Rusticucci, M., Somerville, R., Stocker, T.F., Whetton, P., Wood, R.A. & Wratt, D. (2007). *Technical Summary. In: Climate Change 2007: The Physical Science Basis. Contribution of Working Group I to the Fourth Assessment Report of the Intergovernmental Panel on Climate Change* [S. Solomon, D. Qin, M. Manning, Z. Chen, M. Marquis, K. B. Averyt, M. Tignor, & H. L. Miller, eds.], Cambridge University Press, Cambridge, United Kingdom and New York, NY, USA.

Di Stasio, S., Legarrec, J.L. & Mitchell, J.B.A. (2011). Synchrotron radiation studies of additives in combustion, II: Soot agglomerate microstructure change by alkali and alkaline-earth metal addition to a partially premixed flame. *Energy and Fuels*, 25(3):916–925.

Stohl, A., Klimont, Z., Eckhardt, S., Kupiainen, K., Shevchenko, V.P., Kopeikin, V.M. & Novigatsky, A.N. (2013). Black carbon in the Arctic: The underestimated role of gas flaring and residential combustion emissions. *Atmospheric Chemistry and Physics*, 13(17):8833–8855.

Tappe, M., Haynes, B.S. & Kent, J.H. (1993). The effect of alkali metals on a laminar ethylene diffusion flame. *Combustion and Flame*, 92(3):266–273.

Vengosh, A., Jackson, R.B., Warner, N., Darrah, T.H. & Kondash, A. (2014). A Critical Review of the Risks to Water Resources from Shale Gas Development and Hydraulic Fracturing in

the United States. *Environmental Science & Technology*, 48(15):8334–8348.

Vander Wal, R.L., Choi, M.Y. & Lee, K. (1995). The effects of rapid heating of soot: Implications when using laser-induced incandescence for soot diagnostics. *Combustion and Flame*, 102(1–2):200–204.

Wang, H. (2011). Formation of nascent soot and other condensed-phase materials in flames. *Proceedings of the Combustion Institute*, 33(1):41–67.

Wang, Z., King, S.M., Freney, E., Rosenoern, T., Smith, M.L., Chen, Q., Kuwata, M., Lewis, E.R., Pöschl, U., Wang, W., Buseck, P.R. & Martin, S.T. (2010). The Dynamic Shape Factor of Sodium Chloride Nanoparticles as Regulated by Drying Rate. *Aerosol Science and Technology*, 44(11):939–953.

Wasylishen, R. & Fulton, S. (2012). Reuse of Flowback & Produced Water for Hydraulic Fracturing in Tight Oil. *Pet. Technol. Alliance Can*.

Wersborg, B.L., Yeung, A.C. & Howard, J.B. (1975). Concentration and mass distribution of charged species in sooting flames. *Symposium (International) on Combustion*, 15(1):1439–1448.

Weyant, C.L., Shepson, P.B., Subramanian, R., Cambaliza, M.O.L., Heimburger, A., Mccabe, D., Baum, E., Stirm, B.H. & Bond, T.C. (2016). Black carbon emissions from associated natural gas flaring (web publication). *Environmental Science & Technology*, 50(4):1–24.

Whitaker, S. (1972). Forced Convection Heat Transfer Correlations for Flow In Pipes, Past Flat Plates, Single. *AIChE Journal*, 18(2):361–371.

WHO (2016). Ambient (outdoor) air quality and health. Available at: http://www.who.int/mediacentre/factsheets/fs313/en/.

Zhao, B., Uchikawa, K. & Wang, H. (2007). A comparative study of nanoparticles in premixed flames by scanning mobility particle sizer, small angle neutron scattering, and transmission electron microscopy. *Proceedings of the Combustion Institute*, 31(1):851–860.

Zhao, B., Yang, Z., Johnston, M. V., Wang, H., Wexler, A.S., Balthasar, M. & Kraft, M. (2003a). Measurement and numerical simulation of soot particle size distribution functions in a laminar premixed ethylene-oxygen-argon flame. *Combustion and Flame*, 133(1–2):173–188.

Zhao, B., Yang, Z., Li, Z., Johnston, M. V. & Wang, H. (2005). Particle size distribution function of incipient soot in laminar premixed ethylene flames: Effect of flame temperature. *Proceedings of the Combustion Institute*, 30(1):1441–1448.

Zhao, B., Yang, Z., Wang, J., Johnston, M.V. & Wang, H. (2003b). Analysis of Soot Nanoparticles in a Laminar Premixed Ethylene Flame by Scanning Mobility Particle Sizer. *Aerosol Science and Technology*, 37(8):611–620.

Ziemkiewicz, P.F. & Thomas He, Y. (2015). Evolution of water chemistry during Marcellus Shale gas development: A case study in West Virginia. *Chemosphere*, 134:224–231.

Zolfaghari Sharak, A., Noel, M., Dehghanpour, H. & Bearinger, D. (2014). Understanding the Origin of Flowback Salts : A Laboratory and Field Study. In *SPE/CSUR Unconventional Resources Conference–Canada*. Society of Petroleum Engineers.

Appendix A   Chemical compound of a representative produced water solution

To investigate the effect of produced water on particle emissions from flares a representative solution for produced water needs to be found. Most research papers related to produced water are only focused on the chemical composition of produced water from a specific geographical region. Therefore, it was decided to use a data source with extensive data on produced water from different geographical regions. The United States Geological Survey National Produced Waters Geochemical Database v2.1 (Blondes et al. 2014) provides information on the composition of produced waters sampled from all regions of the United States. This database has information on 161,915 produced water samples and it contains information such as location of the well, date the sample was analyzed, formation type, and chemical species of the produced waters, etc. This database is a collection of 25 individual databases, reports or publications (Blondes et al. 2014). According to the USGS database "the water samples are commonly collected when a well has production problems or during the initial development of a well" (Blondes et al. 2014). Based on their explanation it can be inferred that most of the samples from hydraulically fractured wells could be flowback water rather than produced water. It should also be noted that the USGS data base has a great deal of information on numerous elements (predominately cations and anions) of produced waters. In order to apply data analysis on this database a MATLAB code was used.

A.1 Categorization of Produced Water Sample

The USGS database has several well categories. Conventional hydrocarbon wells and unconventional well types were included. Based on the objective of this project the following well types were investigated:

- Conventional hydrocarbons: Gas and oil that are extracted by the natural pressure of the wells or compression operation, after the drilling process is complete.

- Shale gas: Natural gas which is extracted from low permeability source rocks[3] such as organic-rich shale rocks (Vidic et al. 2013) and shale formations.

- Tight gas: Natural gas extracted from low permeability reservoir rocks (less than 10^2 μm^2) and low porosity (less than 10%) (Jia et al. 2012) where the rock formations are typically sandstones or sometimes limestones.

- Tight oil: Oil that is contained in carbonate rocks and tight sandstone interbedded in the vicinity of source rocks (Jia et al. 2012).

The MATLAB code was used to filter the samples based on the type of wells mentioned. The date of samples in the USGS database is quite extensive and it ranges from 1930 to 2014. However, since the use of horizontal drilling and hydraulic fracturing has been increasingly used in the past decade (Vengosh et al. 2014) it was decided to only include samples since 1990.

A.2 Prominent species in the produced water sample

After categorizing the samples of USGS based on the well type and date, chemical species analysis was conducted to determine which species are common in all of these categories and

---

[3] Rocks that have the capability to produce hydrocarbons or have produced hydrocarbons

which species are measured exclusively in each category. Also for each species the median concentration was determined. The main reason that in the statistical calculation median is used instead of mean is that the concentrations vary by orders of magnitudes; therefore, the mean is highly influenced by the samples with high concentrations. Due to this the mean is not a representative of a frequently occurring sample. The results of the species measured in all well types and species measured only in unconventional wells are shown in A.1 and A.2.

Table A.1. Median concentration (mg/L) of species measured in both conventional and unconventional produced water samples

	Ba	Br	HCO3	Ca	Cl	Fe_{tot}	K	Li	Mg	Na	SO4	Sr
CONV	3	15	300	11300	17800	5	2300	10	1000	91200	1000	50
SG	5	310	1200	120	7000	5000	200	20	20	6000	170	740
TG	10	50	1200	50	3800	10	30	1	8	2800	30	3
TO	60	700	620	7100	75000	41000	4300	40	980	55000	1900	1100

CONV: conventional wells, SG: shale gas, TG: tight gas, TO: tight oil

Table A.2. Median concentration (mg/L) of species only measured in unconventional produced water samples

	NO_2	NO_3NO_2	NH_4	PO_4	S	SO_3	Sn	Ti	Tl	$C_2H_6O_2$	C_3H_6O	C_7H_8	$C_8H_{10\_XY}$	$C_8H_{10\_ETH}$	H_2S	CO_2	OH
SG	3.0	0.3	70	0.2	3.0	12.0	1.0	0.3	0.1	31.0	90	2	114	10	2	260	90
TG	–	–	–	–	–	–	–	–	–	–	–	–	–	–	2	260	0.4
TO	–	–	–	–	–	–	–	–	–	–	–	–	–	–	2	340	–

SG: shale gas, TG: tight gas, TO: tight oil

A secondary purpose of this investigation is to determine "typical" concentrations of important substances which will be used to make a synthetic produced water solution. Based on the number of samples and the median concentration of species, the most prominent chemical species were

selected to be included in the final synthetic produced water solution. These species are Cl, Na, Ca, K, Mg, HCO$_3$ and SO$_4$. The selected species were also included in other chemical analyses of produced water and flowback water in other research (Barbot et al. 2013; Haluszczak et al. 2013; Chapman et al. 2012; Gregory et al. 2011; Hayes & Severin 2012; Horner et al. 2011; Ziemkiewicz et al. 2014).

By further analysis of the datasets obtained after applying the preceding filters (date and well types) it was concluded that the unconventional samples are from specific geographical regions or geological formations. Most of the samples from unconventional databases were from Bakken, Woodford and Wyoming regions; with Bakken mostly consisting of tight oil, Woodford consisting of tight gas and shale gas and Wyoming consisting. On the other hand, since the selected regions are from different parts of the United States the geological formation and rock chemical compositions could be quite different. Therefore, the unconventional well types were categorized based on the above regions and formations. The regional categorization was only applied to unconventional well types. Finally four datasets (Conventional hydrocarbons, Bakken, Woodford, Wyoming) were obtained and further chemical analyses were conducted on these four datasets.

A.3 Dataset Generation Based on Regions and Formations

The MATLAB code was used to produce probability density functions[4] for the concentration of each prominent chemical species in each dataset. It is worth mentioning that in addition to the three regional categories of unconventional wells (Bakken, Woodford, Wyoming), the

---

[4] The parameter used in the y axis of the graphs is $dF/d\log(c_{i+1}/c_i)$ and is the normalized frequency function in logarithmic scale.

probability density functions for the overall unconventional samples are also shown. The results

of these probability density functions are shown in Figures A.1 to A.7.
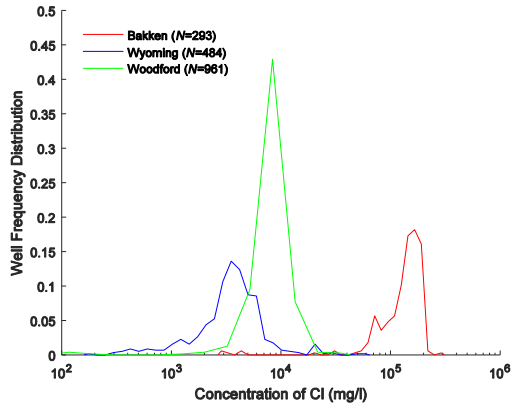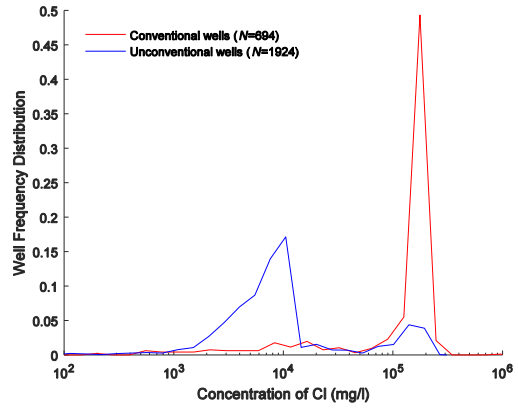
(a)   (b)

Figure A.1. Probability density functions of Cl concentration for (a) unconventional wells and
(b) all conventional and unconventional wells.
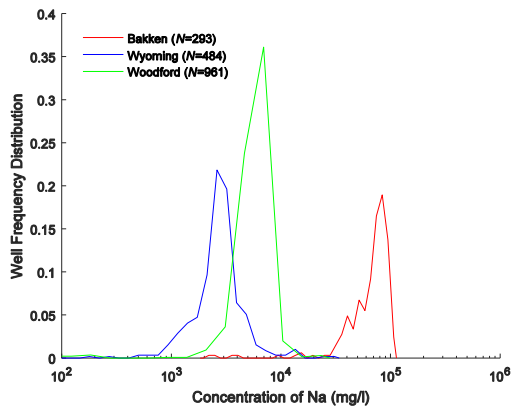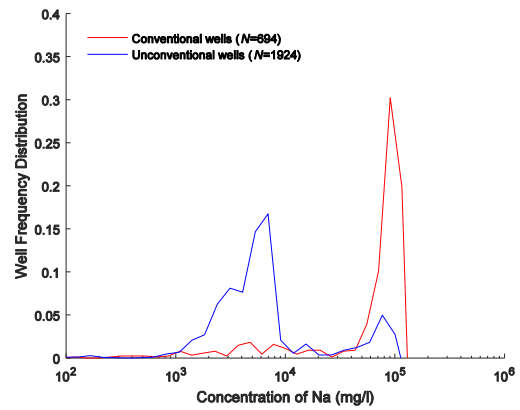
(a)   (b)

Figure A.2. Probability density functions of Na concentration for (a) unconventional wells and (b) all conventional and unconventional wells.
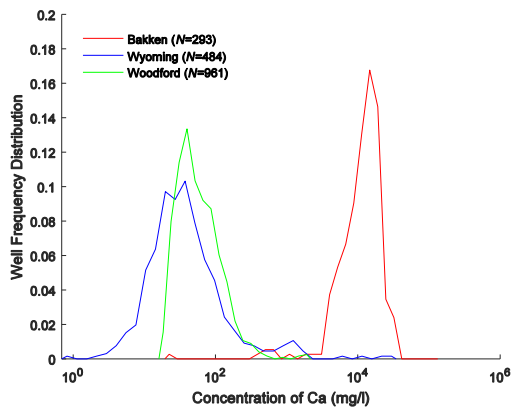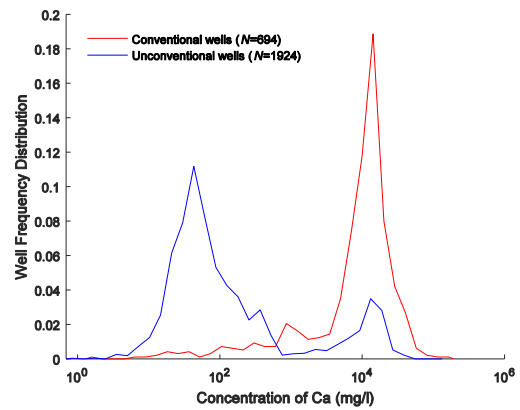
(a)   (b)

Figure A.3. Probability density functions of Ca concentration for (a) unconventional wells and (b) all conventional and unconventional wells.
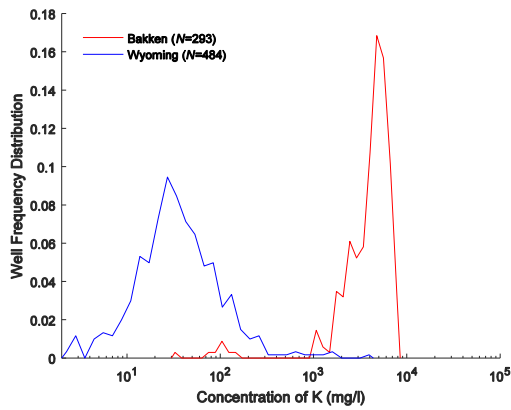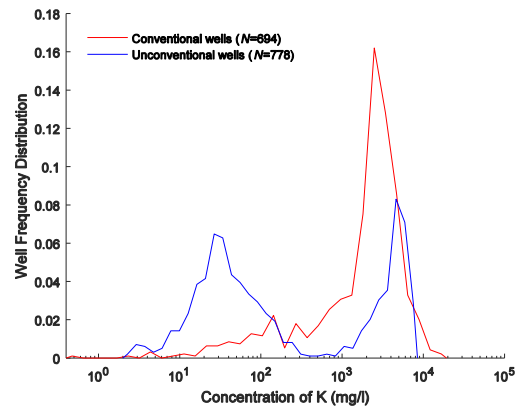
(a)   (b)

Figure A.4. Probability density functions of K concentration for (a) unconventional wells and (b) all conventional and unconventional wells. (Note: No data was available for Woodford).
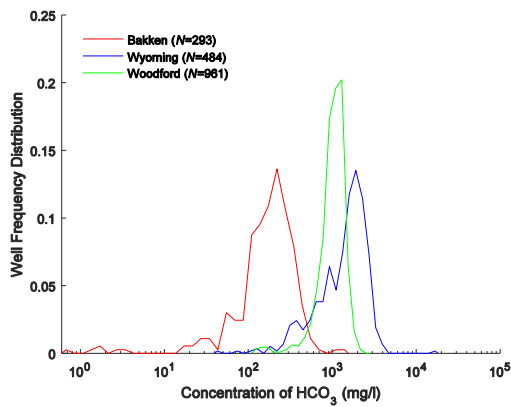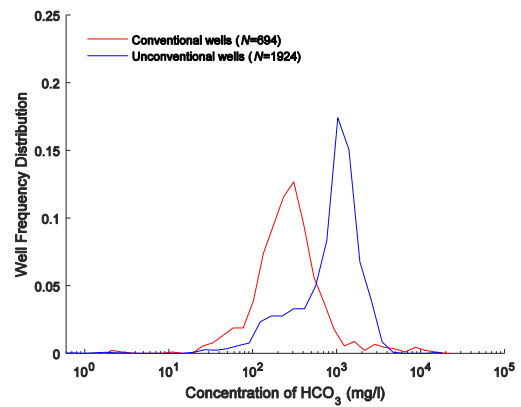
(a)   (b)

Figure A.5. Probability density functions of HCO$_3$ concentration for (a) unconventional wells and (b) all conventional and unconventional wells.
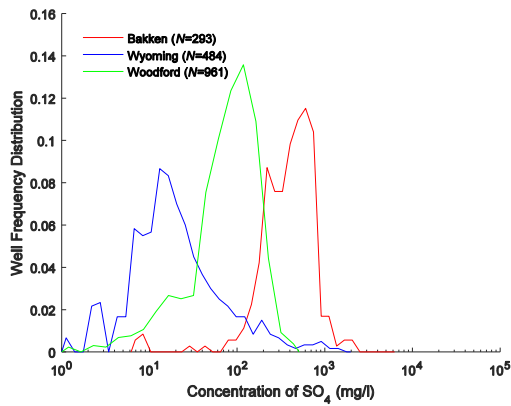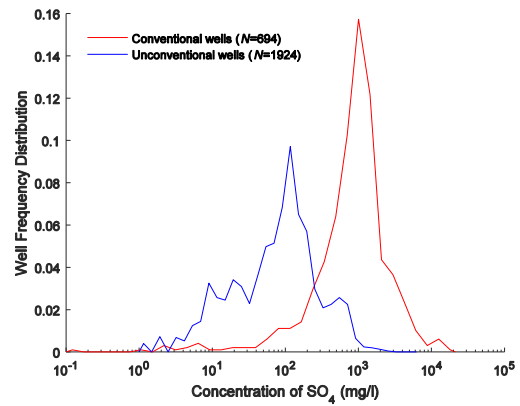
(a)   (b)

Figure A.6. Probability density functions of SO$_4$ concentration for (a) unconventional wells and (b) all conventional and unconventional wells.
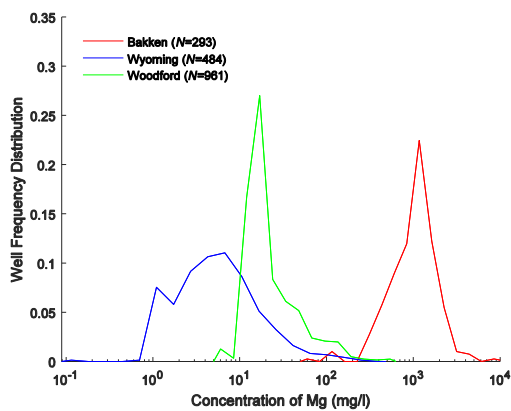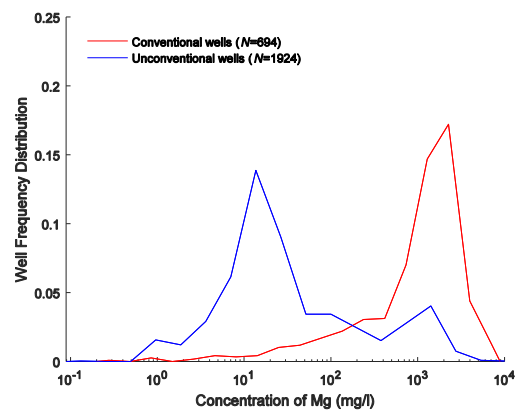
(a)   (b)

Figure A.7. Probability density functions of Mg concentration for (a) unconventional wells and (b) all conventional and unconventional wells.

For each species in each dataset the median was determined. Table A.3 shows the medians of each species in each dataset.

Table A.3. Median concentration (mg/L) of species from selected regions and formations.

Regions and formations	Median concentration (mg/L) based on species						
	Cl	Na	Ca	HCO_3	SO_4	K	Mg
Bakken (293 samples)	145000	73400	12700	180	420	4500	1100
Wyoming (484 samples)	3600	2700	30	1600	20	30	5
Woodford (961 samples)	8500	5774	50	1000	80	–	20
Conventional wells (694 samples)	178000	91200	11300	260	972	2340	1370

A.4 Discussion

The figures show that the conventional hydrocarbon dataset has the highest median concentration of cations (i.e., Na, Ca, K, and Mg) and chlorine. This is likely due to the fact that the produced water from conventional hydrocarbon wells is mostly brine water and it is not diluted with fresh water from the fracturing process. On the other hand, the lowest concentration of cations and chlorine can be found in the Wyoming dataset. Thus, the conventional hydrocarbon dataset can be a representative value of produced water with a high concentration of species, while the results from Wyoming can be treated as a representative value of produced water with low concentration of species.

Comparing these high and low concentration representative with the species concentrations reported in other papers show that the concentration of produced water and flowback water samples measured in other studies are between these two extremes. Table A.4 compares the concentration of species in conventional wells and Wyoming with average flowback water samples from other regions of the United States. Table A.5 compares the concentration of species in conventional wells and Wyoming with average produced water samples from four tight oil resource plays in Alberta and Saskatchewan, Canada.

Most of the reported species concentrations fall between the two cases of conventional wells and Wyoming; therefore, for future work, the synthetic produced water will be based on the concentration of species in those two cases (conventional wells and Wyoming). By applying this assumption, the synthetic produced water must be mixture solution of the salt and acids outlined in Table A.6.

Table A.4. Comparison of conventional well samples and Wyoming with results of Horner et al. (2011).

Species	Concentration (mg/L)				
	Conventional wells	Wyoming	Fayetteville (AR)	Marcellus (PA)	Barnett (TX)
Cl	178000	3600	8042.3	43578.4	23797.5
Na	91200	2700	5362.6	24445	12453
Ca	11300	30	256.3	2921	2242
HCO_3	300	1600	1281.4	261.4	289
SO_4	1000	20	149.4	9.1	60
K	2300	30	–	–	–
Mg	1400	5	77.3	263.1	253

Table A.5. Comparison of conventional well samples and Wyoming with results of (Wasylishen & Fulton 2012).

Species	Concentration (mg/L)					
	Conventional wells	Wyoming	Cardium	Slave Point	Colorado Group	Waskada/Spearfish
Cl	178000	3600	5104	88435	27000	93581
Na	91200	2700	2431	37325	15547	53593
Ca	11300	32	934	11793	641	2551
HCO_3	300	1600	1098	164	463	389
SO_4	1000	20	226	969	152	2104
K	2300	30	169	503	208	585
Mg	1400	5	143	3053	367	746

Table A.6. Chemical compound concentrations in the synthetic produced water for both low and high extremes.

Chemical Compound	Concentration (mg/L)	
	Low extreme (Wyoming)	High extreme (conventional wells)
NaCl	6000	252000
$NaHCO_3$	2100	400
$CaCl_2$	100	31000
KCl	60	4400
MgCl2	0	4500
$MgSO_4$	20	1200

References

Barbot, E., Vidic, N.S., Gregory, K.B. & Vidic, R.D. (2013). Spatial and temporal correlation of water quality parameters of produced waters from Devonian-age shale following hydraulic fracturing. *Environmental Science and Technology*, 47(6):2562–2569.

Blondes, M.S., Gans, K.D., Thordsen, J.J., Reidy, M.E., Thomas, B., Engle, M.A., Kharaka, Y.K. & Rowan, E.L. (2014). U.S. Geological Survey National Produced Waters Geochemical Database v2.1 (PROVISIONAL). *United States Geological Survey*.

Chapman, E.C., Capo, R.C., Stewart, B.W., Kirby, C.S., Hammack, R.W., Schroeder, K.T. & Edenborn, H.M. (2012). Geochemical and strontium isotope characterization of produced waters from marcellus shale natural gas extraction. *Environmental Science and Technology*, 46(6):3545–3553.

Gregory, K.B., Vidic, R.D. & Dzombak, D.A. (2011). Water management challenges associated with the production of shale gas by hydraulic fracturing. *Elements*, 7(3):181–186.

Haluszczak, L.O., Rose, A.W. & Kump, L.R. (2013). Geochemical evaluation of flowback brine from Marcellus gas wells in Pennsylvania, USA. *Applied Geochemistry*, 28:55–61.

Hayes, T. & Severin, B.F. (2012). Barnett and Appalachian Shale Water Management and Reuse Technologies. *Rep. no. 8122-05, Research Partnership to Secure Energy for America*.

Horner, P., Halldorson, B. & Slutz, J. (2011). Shale Gas Water Treatment Value Chain-A Review of Technologies including Case Studies. In *SPE Annual Technical Conference*. Society of Petroleum Engineers.

Jia, C., Zheng, M. & Zhang, Y. (2012). Unconventional hydrocarbon resources in China and the prospect of exploration and development. *Petroleum Exploration and Development*, 39(2):139–146.

Vengosh, A., Jackson, R.B., Warner, N., Darrah, T.H. & Kondash, A. (2014). A Critical Review of the Risks to Water Resources from Shale Gas Development and Hydraulic Fracturing in the United States. *Environmental Science & Technology*, 48(15):8334–8348.

Vidic, R.D., Brantley, S.L. et al., Vandenbossche, J.M., Yoxtheimer, D. & Abad, J.D. (2013). Impact of Shale Gas Development on Regional Water Quality. *Science*, 340(May).

Wasylishen, R. & Fulton, S. (2012). Reuse of Flowback & Produced Water for Hydraulic Fracturing in Tight Oil. *Pet. Technol. Alliance Can*.

Ziemkiewicz, P.F., He, Y. & Quaranta, J.D. (2014). Characterization of Waste Waters from Hydraulic Fracturing. In *Shale Energy Engineering 2014: Technical Challenges, Environmental Issues, and Public Policy*. pp. 63–73.

Appendix B   Mass concentration measurement of injected NaCl particles

As mentioned in Chapter 2, a solution of 25% NaCl (mass based) was injected into the fuel stream. Knowing the concentration of NaCl in the injected solution is not enough to estimate the mass concentration of NaCl particles that are injected into the flame. The first step toward estimating the mass concentration of NaCl particles is to measure the particle size distribution of injected particles from the burner tube. To obtain the PSDs of the NaCl particle, the fuel outlet was connected to the SMPS while NaCl was added to the flow. Figure B.1 shows the PSDs of four SMPS scans of NaCl samples extracted from the burner tube.
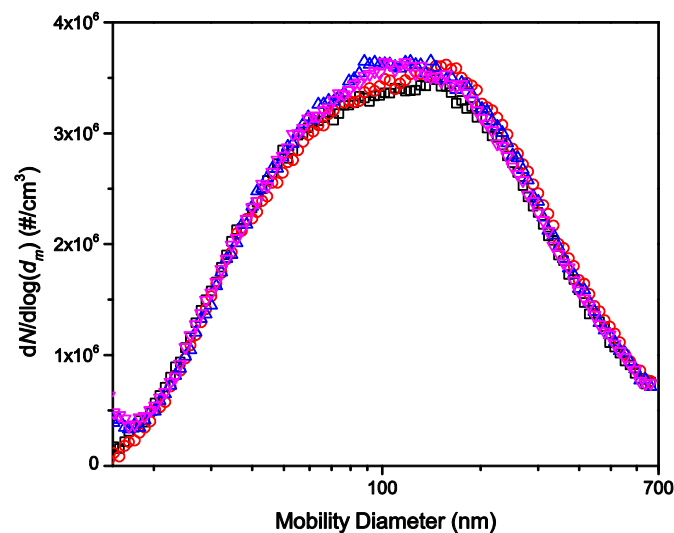
Figure B.1. PSDs of NaCl particles from the burner tubes

The second step in measuring the mass concentration of injected NaCl particle is to determine the mass-mobility function which describes the relationship between mass of particles and their

mobility diameter. To obtain the mass-mobility function a centrifugal particle mass analyzer (CPMA) was added to the components of the SMPS and was placed between CPC and DMA (Figure B.2).
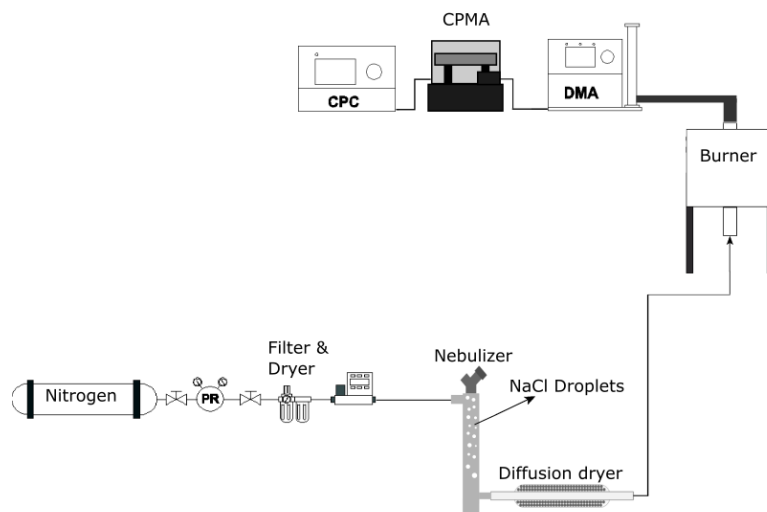
Figure B.2. Scheme of the experimental set-up used from obtaining mass-mobility function.

For estimating the mass-mobility function, the mass of particles were measured at different mobility diameters (38 nm, 50 nm, 65 nm, 98 nm, 146 nm, 219 nm, 329 nm, 494 nm) that cover most of the size range of the injected NaCl particles. This was done by setting the DMA output to a specific mobility diameter, and sending the monodisperse particles into the CPMA and CPC to measure the mass and concentration of particles. Figure B.3 shows the results of m in different mobility diameters.
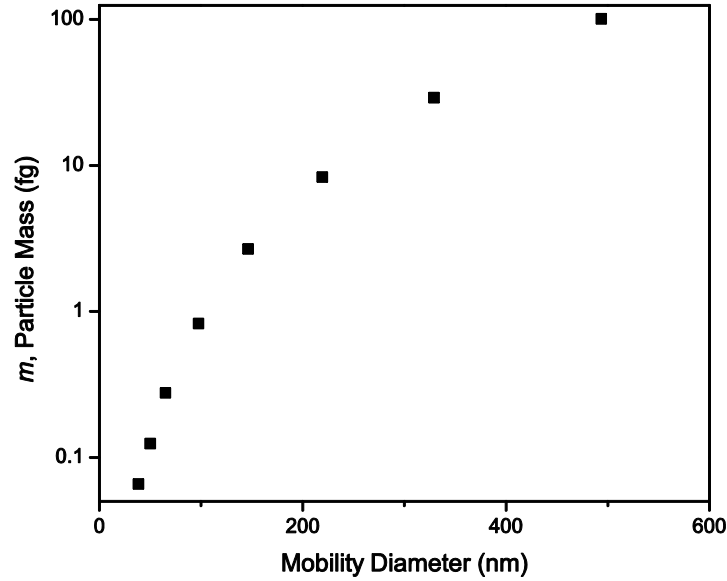
Figure B.3 Mass vs. mobility diameter of NaCl particles

Equation B.1 is the mass mobility function obtained by fitting the experimental data with MATLAB:

$$m(d_m) = 5.7 \times 10^{-07}(d_m)^{3.06} \qquad \text{B.1}$$

The particle size distribution of injected NaCl particles that was measured previously was fitted with a log-normal distribution. Considering the particle size distribution and mass-mobility function the mass concentration of NaCl particles that are inserted into the flame is obtained by the following integral:

$$M_{NaCl} = \int_{0}^{1000} \left(\frac{dN}{dlog(d_m)}\right) m(d_m)dlog(d_m) \qquad \text{B.2}$$

The mass concentration based on Equation B.2 was 49 ng/cm^3. In standard atmospheric conditions the pure methane fuel would have a density of 654000 ng/cm^3, so the mass fraction of the salt is approximately 7e-3%.

Appendix C　　　Uncertainty Analysis

There are three major sources of uncertainty in the experimental measurement that must be investigated. Firstly, the uncertainty associated with temperature measurements and corrections. Secondly, the uncertainty associated with measurements of dilution ratio, and finally the uncertainty of the count median diameter of particles.

C.1 Uncertainty of Temperature Measurements

As different parameters play roles in the measurement of temperature and all of these parameters possess uncertainties, the propagation of the uncertainties of these parameters is needed to derive the overall temperature uncertainty. It was assumed based on (Struk et al. 2003) that the parameters affecting the temperature uncertainties are emissivity, thermocouple bead diameter, Nusselt number and thermocouple temperature measurements.

According to Equation 2.9 the gas temperature is

$$T_g = T_{th} + \frac{\varepsilon \sigma}{Nu}(T_{th}^4 - T_W^4)\frac{d}{k} \qquad\qquad \text{C.1}$$

In these sets of experiment, the temperature was measured at least three times with the thermocouple and the precision uncertainty was calculated for the thermocouple temperature with a 95% confidence. Including the uncertainty of other parameters, the propagation of uncertainties was derived through the following equation:

$$\Delta T_g = \sqrt{(\frac{\partial T_g}{\partial T_{th}}\Delta T_{th})^2 + (\frac{\partial T_g}{\partial \varepsilon}\Delta \varepsilon)^2 + (\frac{\partial T_g}{\partial d}\Delta d)^2 + (\frac{\partial T_g}{\partial Nu}\Delta Nu)^2} \qquad \text{C.2}$$

where ΔT_g is the error of corrected temperature. By taking the derivatives of Eq C.1 we have:

$$(\Delta T_g)^2$$
<div align="right">C.3</div>

$$= ((1 + \frac{4\varepsilon\sigma}{Nu}\frac{d}{k}T_{th}^3)\Delta T_{th})^2 + (\frac{\sigma}{Nu}(T_{th}^4 - T_W^4)\frac{d}{k}\Delta\varepsilon)^2 + (\frac{\varepsilon\sigma}{kNu}(T_{th}^4 - T_W^4)\Delta d)^2$$
$$+ (\frac{\varepsilon\sigma}{Nu\ k}(T_{th}^4 - T_W^4)\Delta d)^2$$

In Equation C.3 ΔT_{th} is the uncertainty associated with thermocouple measurements including both bias and precision uncertainty. $\Delta\varepsilon$ is the uncertainty associated with emissivity. The magnitude of emissivity was adopted from (Miles & Gouldin 1993) and it was mentioned that the uncertainty associated with emissivity is 30%. It is stated in Whitaker (1972) that in the worst case, the Whitaker correlation has a $\pm 30\%$ deviation from experimental data. In our study it is assumed that the uncertainty related to the Nusselt number is $\pm 30\%$. The maximum uncertainty acquired by this method was ± 40.

C.2 Total number Concentration Uncertainties

The total number concentration is the product of dilution ratio and total number concentration of the diluted sample. Thus the main parameters affecting the overall uncertainties are dilution ratio and total number concentration of diluted samples. The first step is to estimate the uncertainty associated with the dilution ratio. From Chapter 2 we know that the dilution ratio is:

$$DR = \frac{X_{CO_2,\ undiluted}}{X_{CO_2,\ diluted}}$$
<div align="right">C.4</div>

Therefore the uncertainty of DR will be:

$$(\frac{\Delta DR}{DR})^2 = (\frac{\Delta X_{CO_2,\ diluted}}{X_{CO_2,\ diluted}})^2 + (\frac{\Delta X_{CO_2,\ undiluted}}{X_{CO_2,\ undiluted}})^2$$
<div align="right">C.5</div>

The $\Delta X_{CO_2, \text{undiluted}}$ is 20 % based on the bias uncertainty of the instrument. By assuming 3 degrees Celsius changes in temperature during the experiments the estimated error associated with $X_{CO_2, \text{diluted}}$ based on the instrument specification is 1.2 ppm.

The formula for total number concentration is:

$$N_{\text{tot},i} = N_{\text{dil}}\, DR \qquad\qquad\qquad\qquad\qquad\qquad\qquad\qquad\qquad\qquad \text{C.7}$$

Where N_{dil}, the total number concentration of diluted sample, is calculated by from its PSD and $N_{\text{tot},i}$ is the total number concentration of ith sample after applying the dilution correction on the PSD. The propagation of uncertainty would lead to the following:

$$(\frac{\Delta N_{\text{tot},i}}{N_{\text{tot},i}})^2 = (\frac{\Delta N_{\text{dil}}}{N_{\text{dil}}})^2 + (\frac{\Delta DR}{DR})^2 \qquad\qquad\qquad\qquad\qquad \text{C.8}$$

The manufacturer of CPC indicated that ΔN_{dil} is 10% and ΔDR is the error of the dilution ratio.

It should be noted that in our experiments the PSDs were calculated at least 3 times and the final demonstrated results and uncertainties are average of these measurements. The maximum uncertainty acquired by this method is $\pm$ 30% of the total number concentration.

C.3 Uncertainty of Count Median Diameter of PSDs

The PSDs from HAB=43 to 60 were fitted by log-normal function. At each height the PSD was measured at least 3 times and the median was measured for each PSD. The total uncertainty of the count median diameter (ΔCMD_t) is due to both biased and precision uncertainties. The

precision uncertainty of the count median diameter (ΔCMD_p) was calculated based on 95% confidence interval. On the other hand, for the bias uncertainty of count median diameter (ΔCMD_b), we have a 3% uncertainty in the instrument (DMA). The total uncertainty of the count median diameter was calculated through the following formula:

$$\Delta CMD_t = \sqrt{(\Delta CMD_p)^2 + (\Delta CMD_b)^2} \qquad \text{C.9}$$

The maximum uncertainty acquired by this method is $\pm$ 10% of the CMD.

References

Miles, P. & Gouldin, F.C. (1993). Determination of the Time Constant of Fine-Wire Thermocouples for Compensated Temperature Measurements in Premixed Turbulent Flames. *Combustion Science and Technology*, 89(1–4):181–199.

Struk, P., Dietrich, D., Valentine, R. & Feier, I. (2003). Comparisons of Gas-Phase Temperature Measurements in a Flame Using Thin-Filament Pyrometry and Thermocouples. In *41st Aerospace Sciences Meeting and Exhibit*.

Whitaker, S. (1972). Forced Convection Heat Transfer Correlations for Flow In Pipes, Past Flat Plates, Single. *AIChE Journal*, 18(2):361–371.

Appendix D   The Adiabatic Flame Temperature for Pure Methane Flame and Methane Flame with NaCl additives

In this study the NaCl particles added to the fuel had a mass concentration of 49 nm/cm^3 and the mass flow rate of the fuel was 0.35 SLPM. To have an estimate of the adiabatic flame temperature in the methane flame condition the mole ratio of NaCl particle to methane is required. The mole flow rate of methane and NaCl is calculated through the following equations:

$$\dot{N}_{\text{NaCl}} = \dot{V}_{\text{CH}_4} \, M_{\text{NaCl}} / MW_{\text{NaCl}} \tag{D.1}$$

$$\dot{N}_{\text{CH}_4} = \dot{V}_{\text{CH}_4} \, \rho_{\text{CH}_4} / MW_{\text{CH}_4} \tag{D.2}$$

where $\dot{V}_{\text{CH}_4}$ the fuel flow rate. By calculation $\dot{N}_{\text{NaCl}}$ and $\dot{N}_{\text{CH}_4}$ the mole ratio of NaCl particle to methane is calculated to be 2.07×10^{-3}. The reaction considered for both cases of pure methane flame and methane flame doped with NaCl particles are as follow:

$$CH_4 + 2(O_2 + 2.76N_2) \rightarrow NaCl_{(g)} + CO_2 + 2H_2O + 5.52N_2 \tag{D.3}$$

$$2.07 \times 10^{-3} NaCl_{(s)} + CH_4 + 2(O_2 + 2.76N_2) \tag{D.4}$$
$$\rightarrow 2.07 \times 10^{-3} NaCl_{(g)} + CO_2 + 2H_2O(g) + 5.52N_2$$
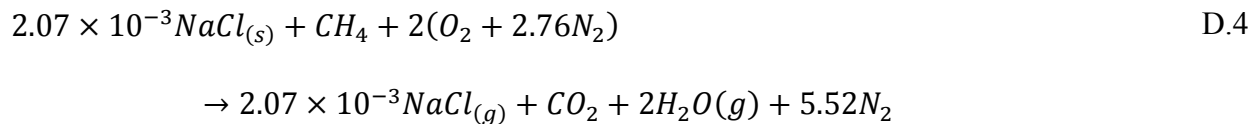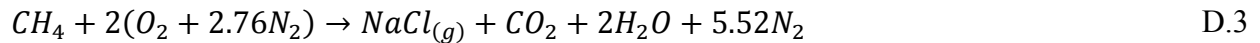
The adiabatic flame temperature for methane diffusion flame was estimated based on the following equations:

$$H_{react} = N_{CH_4}\bar{h}^{\circ}_{f,CH_4} \hspace{6cm} \text{D.5}$$

$$H_{prod} = N_{CO_2}\bar{h}^{\circ}_{f,CO_2} + N_{H_2O}\bar{h}^{\circ}_{f,H_2O} + N_{H_2O}\bar{c}_{p,H_2O}(T_{ad} - 298) \hspace{2cm} \text{D.6}$$

$$+ N_{CO_2}\bar{c}_{p,CO_2}(T_{ad} - 298) + N_{N_2}\bar{c}_{p,N_2}(T_{ad} - 298)$$

In our calculation the specific heat is considered to be constant and the specific heat at 1200 K was considered. This procedure was employed in an example exercise in An Introduction to Combustion (Turns 2000). The adiabatic flame temperature for pure methane calculated is 2317.

For the case of the methane flame doped with NaCl particles the adiabatic flame temperature was calculated by considering the following equations:

$$H_{react} = N_{CH_4}\bar{h}^{\circ}_{f,CH_4} + N_{NaCl}\bar{h}^{\circ}_{f,NaCl_{(s)}} \hspace{4cm} \text{D.7}$$

$$H_{prod} = N_{CO_2}\bar{h}^{\circ}_{f,CO_2} + N_{H_2O}\bar{h}^{\circ}_{f,H_2O} + N_{NaCl}\bar{h}^{\circ}_{f,NaCl_{(g)}} + N_{H_2O}\bar{c}_{p,H_2O}(T_{ad} - 298) \hspace{1cm} \text{D.8}$$

$$+ N_{CO_2}\bar{c}_{p,CO_2}(T_{ad} - 298) + N_{N_2}\bar{c}_{p,N_2}(T_{ad} - 298) + N_{NaCl}(\bar{h}_{NaCl_{(g)}@T_{ad}}$$

$$- \bar{h}_{NaCl_{(g)}@298 \text{ K}})$$

The enthalpy of formation and the enthalpy difference of NaCl were adopted from the website of national institute of standard and technology (NIST 2016). The calculated adiabatic flame temperature under the condition of methane flame doped with NaCl is 2315 K. The calculated results from both cases indicate that the addition of NaCl would not affect the theoretical adiabatic flame temperature under the assumptions considered for the calculations.

References

NIST (2016). sodium chloride. Available at:
http://webbook.nist.gov/cgi/cbook.cgi?ID=C7647145&Mask=1#Thermo-Gas.

Turns, S.R. (2000). *An introduction to combustion: concepts and applications* (2nd ed.), Boston: WCB/McGraw-Hill.